January 2008

Mitigation of Phase Noise at Millimeter-Wave Frequencies for Wireless Personal Area Network Applications

Abdul Ashik Abdul Waheed
University of Massachusetts Amherst

MITIGATION OF PHASE NOISE AT MILLIMETER-WAVE FREQUENCIES FOR WIRELESS PERSONAL AREA NETWORK APPLICATIONS

A Thesis Presented

by

ABDUL ASHIK ABDUL WAHEED

Submitted to the Graduate School of the
University of Massachusetts Amherst in partial fulfillment
of the requirements for the degree of

MASTER OF SCIENCE IN ELECTRICAL AND COMPUTER ENGINEERING

September 2008

Electrical and Computer Engineering

MITIGATION OF PHASE NOISE AT MILLIMETER-WAVE FREQUENCIES FOR WIRELESS PERSONAL AREA NETWORK APPLICATIONS

A Thesis Presented

by

ABDUL ASHIK ABDUL WAHEED

Approved as to style and content by:

_____
Dev Vrat Gupta, Chair

_____
Patrick Kelly, Member

_____
Dennis Goeckel, Member

_____
Christopher V. Hollot, Department Head
Electrical and Computer Engineering

ACKNOWLEDGEMENTS

I would like to thank my advisor, Professor Dev Vrat Gupta, for all his guidance and assistance throughout the duration of this project. Thanks to my committee members Professor Dennis Goeckel and Professor Patrick Kelly for their continuous support and guidance throughout my graduate school. I would also like to thank Dr. Zhiguo Lai for his enlightening critique in many aspects of the project and for the essential comments concerning this document. Thanks and appreciation goes to all my teachers, family and friends.

ABSTRACT

MITIGATION OF PHASE NOISE AT MILLIMETER-WAVE FREQUENCIES FOR WIRELESS PERSONAL AREA NETWORK APPLICATIONS

SEPTEMBER 2008

ABDUL ASHIK ABDUL WAHEED
B.E., ANNA UNIVERSITY, CHENNAI
M.S.E.C.E., UNIVERSITY OF MASSACHUSETTS AMHERST

Directed by: Professor Dev Vrat Gupta

This thesis project discusses the possible transmission at a data rate of several Gbps at millimeter-wave frequencies (e.g., 60 GHz) impaired by oscillator phase noise which is expected at the gigahertz range of frequencies. The thesis briefly describes the phase noise, its mathematical models, and its effect on various standard digital modulation schemes through theoretical phase noise analysis and numerical simulations. A suitable modulation scheme for mitigating the effect of phase noise is then examined. This method employs the pulse amplitude modulation with dual-rail bipolar (DRB) signaling. A single-sideband signal is transmitted along with a low power pilot, which is recovered at the receiver as a local oscillator using narrow band pass filter (NBPF). The design of the NBPF is considered and an analysis of the effect of the bandwidth of the NBPF on the phase noise performance of the DRB system is done to appropriately choose the bandwidth depending on the phase noise requirements.

The numerical simulation results of the examined DRB system show that this scheme has a better BER performance than QPSK and QAM-16 schemes for high phase noise powers of -85dBc/Hz and above even without a required delay line in the signal path. We compare the BER performance of the DRB scheme with an uncompensated QPSK system since both of them have spectral efficiency of approximately 2bps/Hz.

Further simulations with an ideal delay line and ideal Hilbert transform in the signal path show that the BER performance becomes even better than the case without delay line. Hence the design of a delay line and the Hilbert transform at the receiver end over a bandwidth of 1GHz is also considered though these are not actually used in the simulation and left as future work. The effect of the tolerance values of the passive components is considered and a standard method for electronically tuning the circuits using varactor ICs is suggested to neutralize this effect. An investigation of the use of costas loop in the presence of phase noise is also done only to show that at gigahertz frequency range a low cost costas loop is not effective at eliminating the phase noise which is confirmed by the simulation results.

TABLE OF CONTENTS

LIST OF FIGURES

Figure Page

CHAPTER 1

INTRODUCTION

A WPAN (wireless personal area network) is a personal area network for interconnecting devices centered on an individual person's workspace - in which the connections are wireless. Typically, WPAN networks focus on applications which use some technology that permits communication within a relatively short transmit distance (10-30 meters) and high data rate (480Mbps-2Gbps) [49], [50].

A WPAN could serve to interconnect all the ordinary computing and communicating devices that many people have on their desk or carry with them today - or it could serve a more specialized purpose such as allowing the surgeon and other team members to communicate during an operation. A key concept in WPAN technology is known as *plugging in*. In the ideal scenario, when any two WPAN-equipped devices come into close proximity (within several meters of each other) or within a few kilometers of a central server, they can communicate as if connected by a cable. Another important feature is the ability of each device to lock out other devices selectively, preventing needless interference or unauthorized access to information.

The proliferation of mobile computing devices including laptops, personal digital assistants (PDAs), and wearable computers has created a demand for WPANs. The mobile nature of these devices places unique requirements on PANs, such as low power consumption, frequent make-and-break connections, resource discovery and utilization, and international regulations. The technology for WPANs is undergoing rapid development. The objective is to facilitate seamless operation among home or business devices and systems. For example, WPANs may be used to connect PDAs to printers, headsets to cell phones, and PCs to wireless mice and keyboards.

Due to the increased demand for high speed applications, of data rate at least 1 Gbps like the high speed internet access, streaming content downloading (video on demand, HDTV, home theater, etc.), real-time streaming and wireless data bus for cable replacement, WPAN systems providing broadband wireless access such as ultra wideband (UWB) are being seriously considered over the recent years. The task group TG3c under IEEE 802.15 working group, which has charge of standardizing WPAN

systems, e.g., the UWB system, is now intensively discussing future WPAN systems, IEEE 802.15.3c, which operates in the 60 GHz millimeter-wave band [2]. The unoccupied millimeter-wave spectrum (roughly from 57 GHz to 64 GHz) has been allocated for WPAN applications.

To achieve the maintenance of coordination between the mobile nodes in the WPAN under unpredictable conditions like fast movement of the nodes, there is a necessity for fast and seamless switching between the nodes and also very fast tracking and locking time between the nodes. In the case of carrier recovery loops (costas or squaring), there is always significant tracking time (of the order of ms) at such high speed whenever the nodes want to switch amongst them to communicate with each other. This decreases the performance of the overall system.

As clock speeds in communications systems move onto the gigahertz range, phase noise pose a major problem. Phase noise is a vital issue in analog designs and is becoming increasingly critical to the performance of digital chips and boards. Timing errors in the clock or oscillator waveforms of high-speed systems can limit the maximum speed of a digital I/O interface, increase the bit error rate of a communications link, or even cap the dynamic range of an A/D converter.

During the past decade, phase noise received intense attention from researchers in various fields ranging from analog/RF circuit design and computer-aided design [1], to optical/wireless communications and applied mathematics [3]. One can now say that a good theoretical and practical understanding of phase noise in oscillators and phase-locked loops has been achieved. However despite the tremendous progress on the theory, modeling, analysis, and characterization of phase noise [6], [11] there has been no comprehensive scheme which reduces the bit error rate caused by phase noise to an arbitrarily small value. [51] shows how QPSK is unable to support 2Gbps data rate when the phase noise level is above -85dBc/Hz.

Over the years, many researchers have investigated the error performance of binary phase shift keying (BPSK) and differential PSK (DPSK) systems over an additive white Gaussian noise (AWGN) channel in the presence of noisy phase reference [29]-[35]. For BPSK systems, [36] [41] have evaluated the bit error rate (BER) in the presence of Rayleigh fading and noisy phase reference. The corresponding error performance in Rician and Lognormal fading channels have also been investigated in [36] and [40].

The incorporation of the effect of phase noise on the bit error probability, P_E, is as follows for all the abovementioned work:

$$P_E = \int_{-\pi}^{\pi} P(E \mid \phi) f_\phi(\phi) d\phi \tag{1}$$

where $f_\phi(\phi)$ is the probability density function (PDF) of the carrier recovery loop phase error ϕ and $P(E \mid \phi)$ is the conditional bit error probability on the PDF of ϕ. For ϕ constant over the bit duration and a perfect demodulator for BPSK,

$$P(E \mid \phi) = \frac{1}{2} erfc[\sqrt{\rho}\cos(\phi)] \tag{2}$$

where ρ is the received E_b / N_0 .

The effect of an imperfect reference on BPSK systems with a carrier recovery loop (either Squaring or Costas) has been analyzed and predicted by Lindsey [42]-[44], Stiffler [45], Prabhu [46], Holmes [47] and others. In the case of first order the exact solution for the PDF of the phase error turns out to be Tikhonov distribution (also called Truncated Gaussian). For second order PLL Lindsey [42]-[44], considers it truncated Gaussian and Stiffler [45] considers it Gaussian.

Tikhonov PDF is given by

$$f_\phi(\phi) = \frac{e^{\alpha\cos(\phi)}}{2\pi I_0(\alpha)}, -\pi < \phi < \pi \tag{3}$$

where α is the signal-to-noise ratio (SNR) in the first-order phase locked loop and I_0 is the modified Bessel function of order 0. Figure 1 shows the effect of carrier synchronization jitter upon a BPSK receiver with a first order carrier loop assuming Tikhonov PDF for phase error. To compute the performance curves in Figure 1, we substitute Equations (2) and (3) in Equation (1),

$$P_E(\rho) = \int_{-\pi}^{\pi} \frac{1}{2} erfc[\sqrt{\rho}\cos(\phi)] \frac{e^{\alpha\cos(\phi)}}{2\pi I_0(\alpha)} d\phi \tag{4}$$

We see from Figure 1 that as phase noise increases, BER also increases.

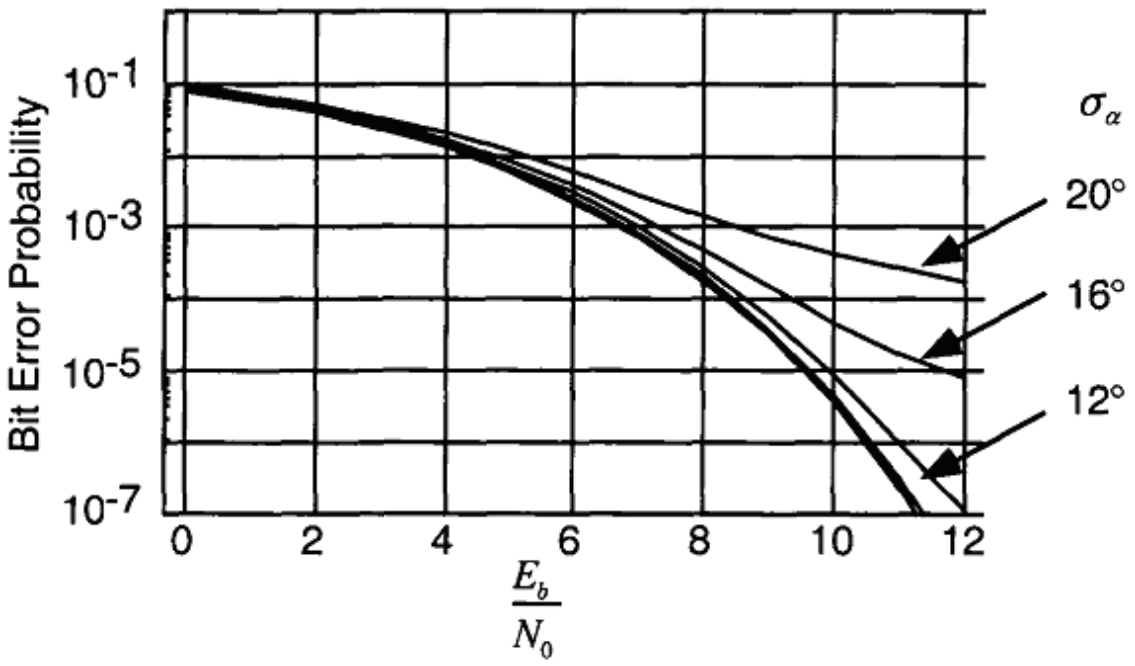

Figure 1 Effect of carrier synchronization jitter on a BPSK receiver with costas loop

Over the last few years, research has been going on to build low phase noise voltage-controlled oscillators [21] operating at GHz frequency range. Low-phase-noise oscillators were demonstrated [22]–[28] at 4-70 GHz with phase noise of the order of -110 dBc/Hz (1 MHz offset) using technologies like CMOS, SiGe BiCMOS, GaInP/GaAs HBT. But these products are still in the research stage only and not commercial. Further they are too expensive to build. The objective of this thesis is to show how phase noise affects the performance of digital communications systems employing various modulation schemes. Then we proceed on to develop suitable channel encoding and modulation schemes to mitigate the effect of phase noise. To satisfy the technical requirements of WPAN such as high throughput and low power consumption, it is necessary to design a low complexity modulation and detection algorithm for 60 GHz WPAN.

This thesis is organized as follows. In Chapter 2 we give a brief description of phase noise and its mathematical models and then show its effect on various modulation schemes through numerical simulation results. We also discuss the effectiveness of Costas receivers and PLLs in the presence of phase noise through simulation results of BPSK Costas receiver. We then examine in Chapter 3 a simple modulation scheme to

mitigate the phase noise effect. The examined system employs the pulse amplitude modulation (PAM) with a dual-rail bipolar signaling and will be referred to as the dual-rail bipolar modulation throughout this document. We then show the simulations results of this system in the presence of phase noise. Chapter 4 summarizes the work done and the possible future research work.

CHAPTER 2

PHASE NOISE

2.1 What Is Phase Noise?

Oscillator phase noise has long been the subject of theoretical and experimental investigation. It refers to the short-term random fluctuations in the frequency (or phase) of an oscillator signal. Consider an ideal sinusoidal oscillator. Its output may be expressed as

$$V_o(t) = V_0 \cos(2\pi f_0 t + \phi), \tag{5}$$

where V_0 is the amplitude, f_0 is the angular frequency and ϕ is an arbitrary, fixed phase reference. Therefore the spectrum of an ideal oscillator is an impulse at f_0 as shown in Figure 2 (a). In a practical oscillator, however, the output is more generally given by

$$V_o(t) = V_0[1 + A(t)]\cos[2\pi f_0 t + \phi(t)] + \text{high order harmonics}, \tag{6}$$

where $A(t)$ and $\phi(t)$ represent time-dependent amplitude and phase fluctuations of the signal, respectively. As a consequence, the spectrum of a practical oscillator has sidebands distributed around the center frequency, f_0, as shown in Figure 2 (b). Note that there are usually two types of phase terms appearing at the output spectrum of the oscillator (other than the high order harmonics). The first type appears as a distinct component in the spectrum and it is referred to as a *spurious tone*. The second type appears as random phase fluctuations and is referred to as *phase noise*.

2.2 Effects of Phase Noise on Receiver Performance

Typical distortions caused by phase noise are phase jitter and reciprocal mixing, which can degrade both the bit error rate and the selectivity of a receiver.

As will be seen in the next section, the phase noise adds a random error to the received signal's phase, resulting in the shifts in the position of constellation points. Such shifts can show up in the bit error rate of the demodulated signal and can be disastrous for complicated constellations such as 16-QAM.

Reciprocal mixing refers to the process of degradation to the desired signal caused by conversion of neighboring channel energy into the desired signal's bandwidth. This problem is particularly severe in multi-carrier systems where the carriers are closely spaced in frequency. The resulting spectrum is a consequence of simultaneously mixing the desired signal with an interfering signal.

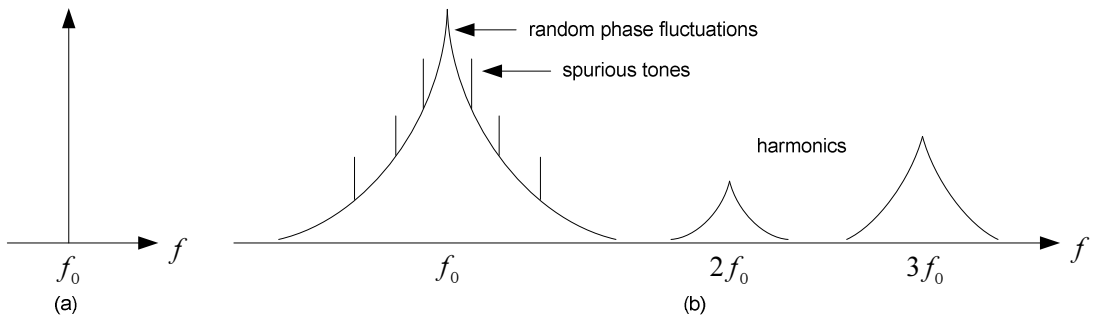

Figure 2 The oscillator output spectrum: (a) ideal , (b) practical.

2.3 Phase Noise Models

The phase noise of an oscillator is typically quantified by the single-sideband (SSB) phase noise, which is defined as the ratio of noise power, P_{noise}, in a 1 Hz bandwidth at an offset f_m from the fundamental signal frequency, to the signal power, P_{signal}, as shown in Figure 3.

$$L(f_m) = 10 \cdot \log_{10}\left[\frac{P_{\text{noise}}(f_m, 1\,\text{Hz})}{P_{\text{signal}}}\right], \tag{7}$$

An early model of phase noise, introduced by Leeson [6], is based on a linear time-invariant approach to the analysis of noise in oscillators and is given as

$$L(f_m) = 10 \cdot \log_{10}\left[\frac{FkT}{P_{\text{signal}}}\left\{1+\left(\frac{f_0}{2Qf_m}\right)^2\right\}\left(1+\frac{f_{1/f^3}}{f_m}\right)\right], \tag{8}$$

where F is an empirical parameter, k is Boltzmann's constant, T is the temperature in Kelvin, Q is the quality factor of the resonator LC-tank and f_{1/f^3} is the corner frequency between the $1/f_m^3$ and $1/f_m^2$ regions, as shown in Figure 4 (where both the horizontal and vertical axes are in logarithmic scale).

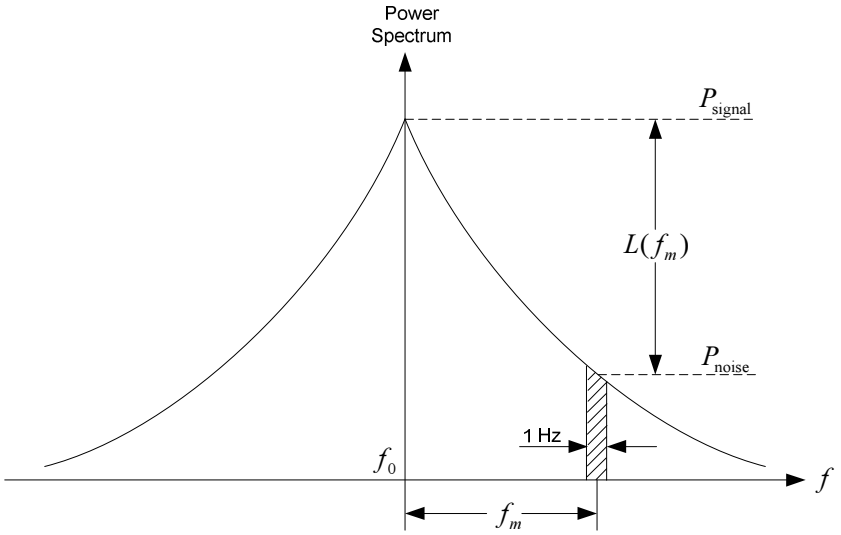

Figure 3 Phase noise definition.

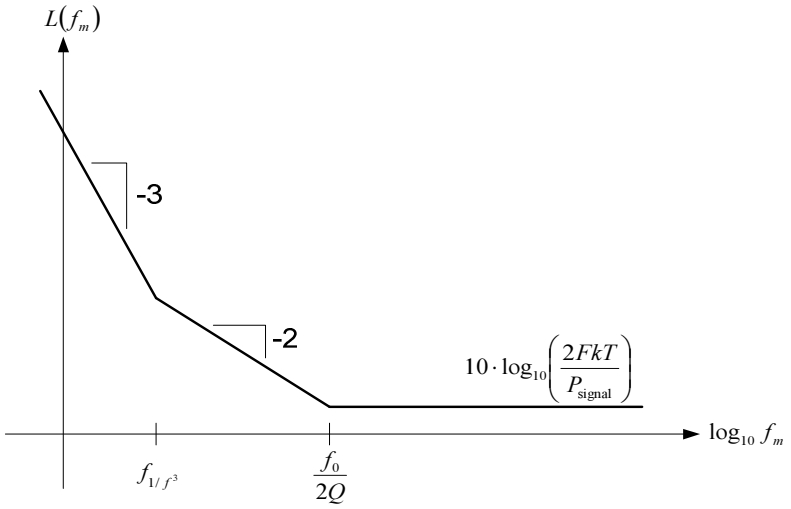

Figure 4 Leeson's model of phase noise.

Despite its limitations and drawbacks [6], Leeson's model involves some key parameters and is extremely valuable for the intuitive insights it may provide about oscillators. Other models such as those developed by Hijimira and Lee [9], Rael and Abidi [15], and Razavi [16] are available in the literature and will not be explained here. In this thesis, we consider the phase noise model adopted by IEEE 802.15.3c task group [2],

$$L(f_m) = L(0) \cdot \frac{1 + (f_m / f_z)^2}{1 + (f_m / f_p)^2}, \tag{9}$$

where the zero frequency, f_z, and the pole frequency, f_p, are taken to be 1 MHz and 100 MHz, respectively. Figure 5 shows a plot of $L(f_m)$ with $L(0) = -90$ dBc/Hz. The red dashed curve is the given model and the blue curve is the simulated one (which will be further explained in the next section).

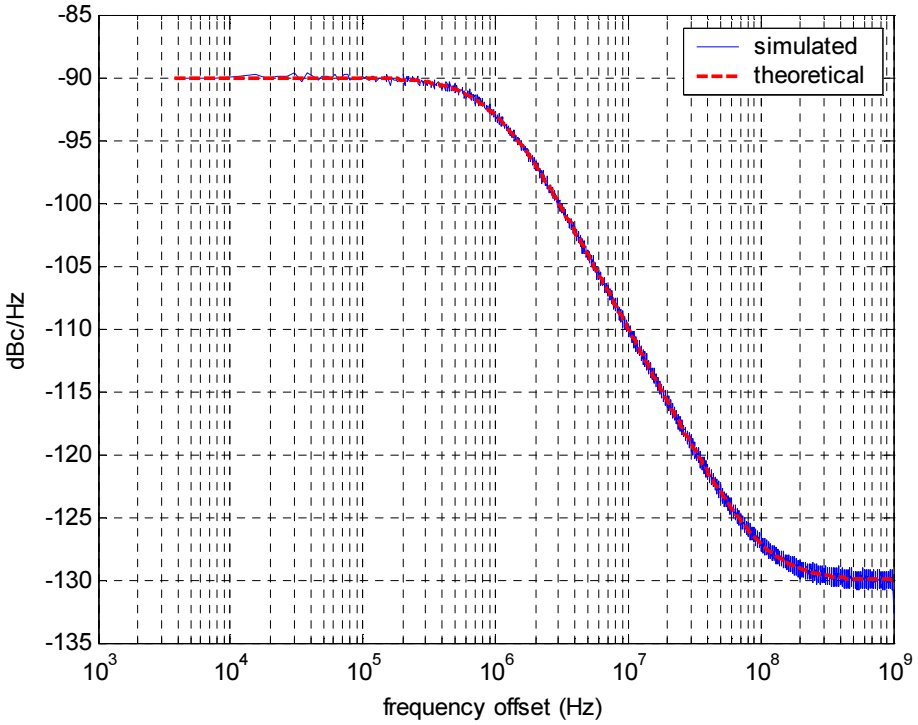

Figure 5 Phase noise model adopted by IEEE 802.15.3c task group.

2.4 Theoretical Phase Noise Analysis of the IEEE Model

Figure 6 shows the effect of carrier synchronization jitter upon a BPSK receiver without a carrier loop. The phase noise at the output of the demodulator is given by $\phi(t) = \phi_{TX}(t) - \phi_{RX}(t)$ where $\phi_{TX}(t)$ and $\phi_{RX}(t)$ are introduced at the transmitter and receiver side local oscillators, respectively.

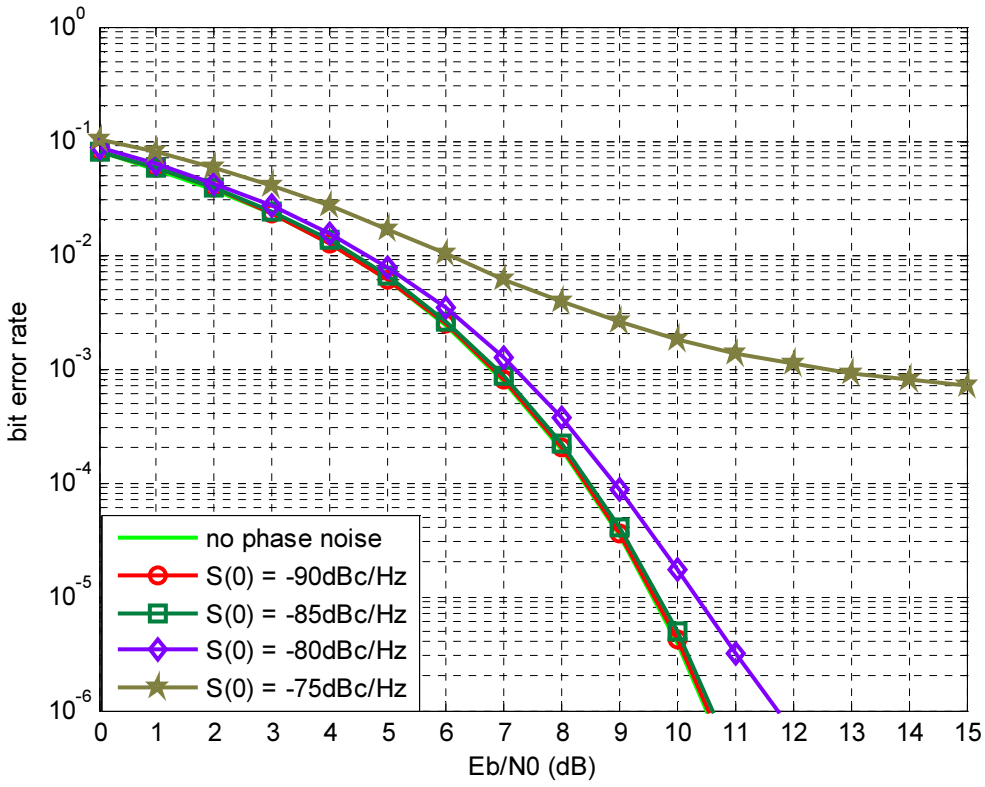

Figure 6 Analytical bit error rate performance of BPSK with phase noise

Let us assume ϕ_{TX} and ϕ_{RX} have approximately Gaussian distribution with mean zero and variance $\sigma^2 = 2\int_0^\infty S_\phi(f)df$ where S_ϕ(f) is the power spectral density of phase noise given in Figure 5. Hence we can assume ϕ is also approximately Gaussian distributed with mean zero and variance $2\sigma^2$ with probability density function,

$$f_\phi(\phi) = \frac{e^{-\phi^2/4\sigma^2}}{2\sqrt{\pi}\sigma}, -\pi < \phi < \pi \tag{10}$$

To compute the performance curves in Figure 6, we substitute Equations (2) and (10) in Equation (1),

$$P_E(\rho) = \int_{-\pi}^{\pi} \frac{1}{2} erfc[\sqrt{\rho}\cos(\phi)] \frac{e^{-\phi^2/4\sigma^2}}{2\sqrt{\pi}\sigma} d\phi \tag{11}$$

2.5 Simulation Results

In this section we show simulation results for various digital modulation schemes in the presence of phase noise of different power levels. Throughout this thesis, only AWGN channel is considered.

2.5.1 System Block Diagram

Three modulation schemes, BPSK, QPSK, and 16-QAM, are considered. Figure 7 shows the system block diagram. Mathematically the transmitted signal for these three schemes can all be represented by one equation

$$s_c(t) = \sum_k g(t - kT)\left\{a_{Ik}\cos\left[2\pi f_c t + \phi_{\mathrm{TX}}(t)\right] - a_{Qk}\sin\left[2\pi f_c t + \phi_{\mathrm{TX}}(t)\right]\right\} \tag{12}$$

where a_{Ik} and a_{Qk} are the in-phase and quadrature components, respectively, T is the symbol interval, $g(t)$ is the signal pulse, f_c is the carrier frequency, and $\phi_{\mathrm{TX}}(t)$ is the phase noise (in time-domain) from the oscillator at the transmitter end. Assuming perfect image rejection and bandpass filtering, signals fed to the matched filters at the receiver are

$$y_{\mathrm{I}}(t) = r(t)\cos\left[2\pi f_c t + \phi_{\mathrm{RX}}(t)\right] = \left[s_c(t) + n(t)\right]\cos\left[2\pi f_c t + \phi_{\mathrm{RX}}(t)\right] \tag{13}$$

and

$$y_{\mathrm{Q}}(t) = r(t)\sin\left[2\pi f_c t + \phi_{\mathrm{RX}}(t)\right] = \left[s_c(t) + n(t)\right]\sin\left[2\pi f_c t + \phi_{\mathrm{RX}}(t)\right] \tag{14}$$

where $n(t)$ is the additive white Gaussian noise and $\phi_{\mathrm{RX}}(t)$ is the phase noise (in time-domain) from the oscillator at the receiver end.

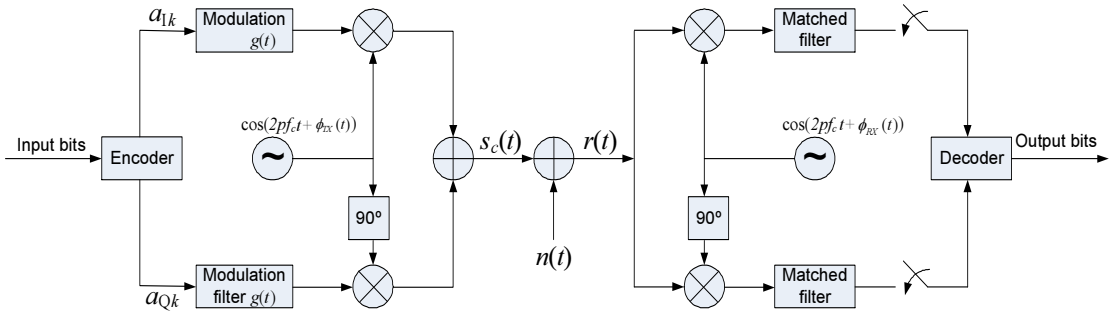

Figure 7 System block diagram.

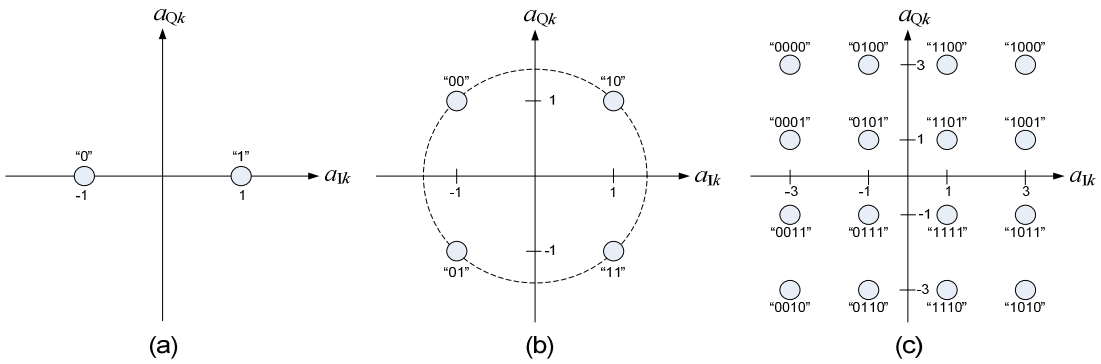

Figure 8 Signal-space diagrams for (a) BPSK, (b) QPSK, and (c) 16-QAM

Note that the ordered pairs (a_{Ik}, a_{Qk}) represent constellation points in the signal-space diagram. They are chosen to follow the Gray coding rules [7] as shown in Figure 8.

2.5.2 Pulse Shaping

To improve the spectral efficiency and meanwhile to minimize the inter-symbol interference (ISI), the signal pulse $g(t)$ is taken to be a square-root raised-cosine pulse (SRRC) [14],

$$g(t) = \frac{\sin\left[\frac{\pi t}{T}(1-\beta)\right] + \frac{4\beta t}{T}\cos\left[\frac{\pi t}{T}(1+\beta)\right]}{\frac{\pi t}{T}\left[1-\left(\frac{4\beta t}{T}\right)^2\right]}, \tag{15}$$

where $0 \le \beta \le 1$ is the roll-off factor. The corresponding spectrum is given by

$$G(f) = \begin{cases} 1 & 0 \le |f| \le \frac{1-\beta}{2T} \\ \sqrt{\frac{1}{2}\left\{1+\cos\left[\frac{\pi T}{\beta}\left(|f|-\frac{1-\beta}{2T}\right)\right]\right\}} & \frac{1-\beta}{2T} \le |f| \le \frac{1+\beta}{2T} \\ 0 & |f| \ge \frac{1+\beta}{2T} \end{cases} \tag{16}$$

Figure 9 shows an example of such pulse in both time- and frequency-domains. Note that the time-domain signal is truncated and shifted so that it is causal and physically realizable.

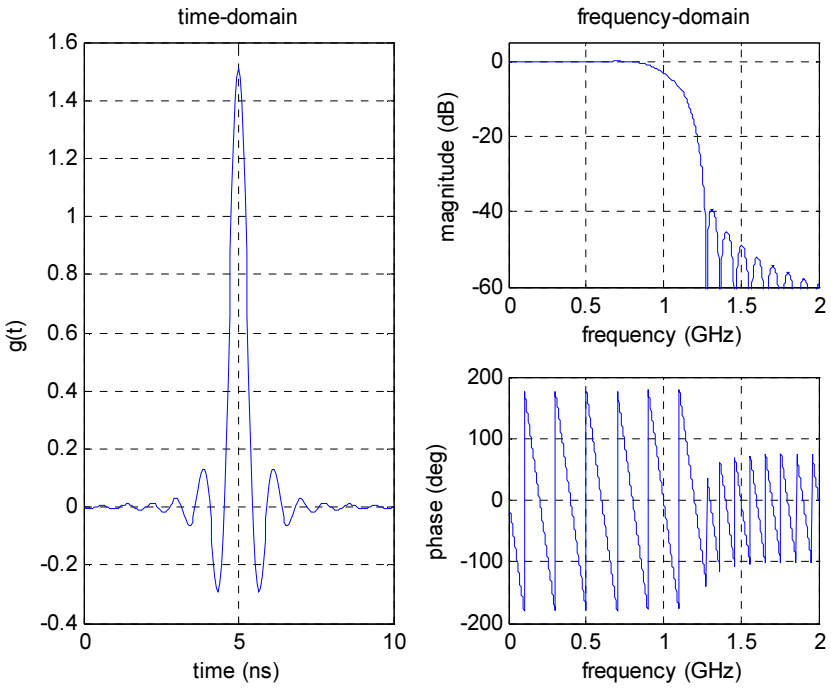

Figure 9 Square-root raised-cosine pulse with $T = 0.5$ ns and $\beta = 0.25$.

2.5.3 Numerical Generation of Phase Noise

To generate the phase noise in time-domain, consider a low pass analog filter whose impulse response is given by

$$H(s) = \frac{1 + s/2\pi f_z}{1 + s/2\pi f_p}, \tag{17}$$

where f_z and f_p are the zero and pole frequencies given in the phase noise model (9). Passing a white Gaussian noise with power spectral density $L(0)$ through such a filter, the output spectrum $Y(f)$ is simply [13]

$$Y(f) = L(0) \cdot \left| H(s) \right|^2_{s=j2\pi f} = L(0) \cdot \frac{1 + \left(f / f_z \right)^2}{1 + \left(f / f_p \right)^2}, \tag{18}$$

which is exactly same as the phase noise model given in equation (9). The white Gaussian noise can be easily generated available computer routines such as Matlab command **`WGN`**. So all we need to do is to design a digital filter corresponding to the analog filter given in (17), which can be implemented using any of a few standard

procedures such as impulse invariance method and bilinear transformation [12]. An example of the generated phase noise is shown in the Figure 10.

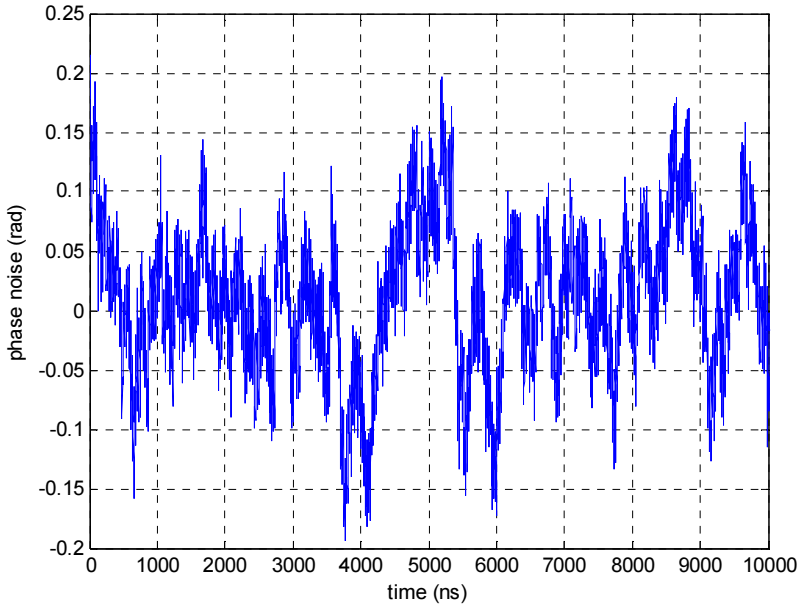

Figure 10 An example of phase noise in time-domain.

2.5.4 BER performance of uncompensated BPSK, QPSK and QAM-16

Figures Figure 11 to Figure 13 show the bit error rate performance of BPSK, QPSK, and 16-QAM in the presence of phase noise. All simulations use a symbol interval of 0.5ns (or equivalently a data rate of 2Gbps) and a roll-off factor of 0.25 for the square-root raised-cosine pulse. One hundred packets of size 2kB (about 1.6×10^6 bits) are transmitted. Four levels of phase noise power are considered. The analytical curves in these figures follow from the equations given below [7]:

$$P_b = Q\left(\sqrt{\frac{2E_b}{N_0}}\right) \quad \text{for BPSK or QPSK}$$
$$P_b = \frac{3}{4}Q\left(\sqrt{\frac{4E_b}{5N_0}}\right) \quad \text{for } 16\text{-QAM} \qquad (19)$$

where E_b / N_0 is the signal-to-noise ratio per bit. From these figures, we see that as the phase noise power level increases, the bit error rate increases sharply to high values as expected, especially in the case of 16-QAM.

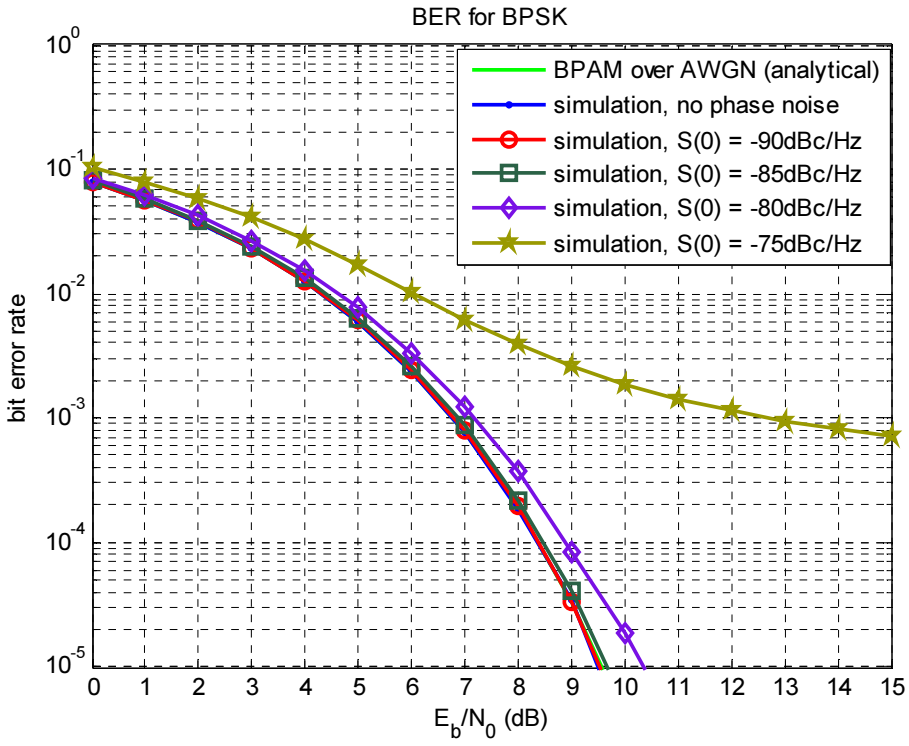

Figure 11 BER performance of BPSK in the presence of phase noise.

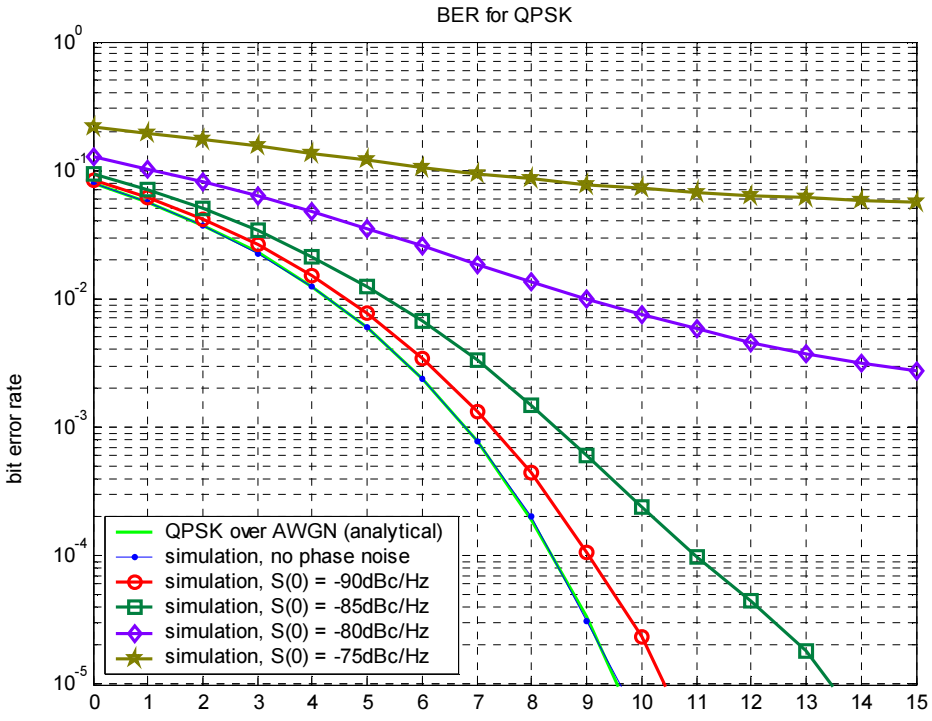

Figure 12 BER performance of QPSK in the presence of phase noise.

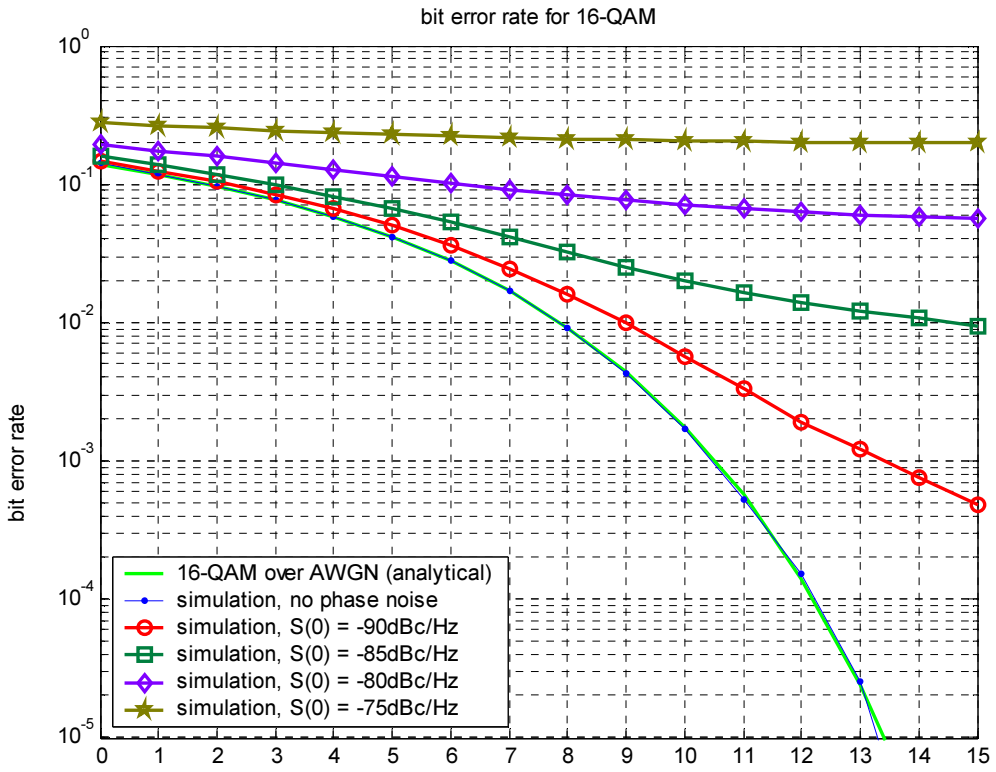

Figure 13 BER performance of 16-QAM in the presence of phase noise.

To gain more insight to the effect of phase noise, we show in Figure 14 the scatter plots (left column) and the eye diagrams (right column) of the demodulated QPSK signal. The channel noise is set to zero when running these simulations. Figure 14 (a) shows the results when no phase noise is present. The scatter plot is perfect and the eye is 100% open at the center. Figure 14 (b) shows the results for a phase noise power level of -85dBc/Hz. We can see that the phase noise adds a random error to the signal's phase, so that the constellation points in the scatter plot spread in a radial pattern around the origin and error occurs when the points cross the decision regions (for QPSK, error occurs if the phase is changed by more than 45 degrees). As for the eye diagram, we can see that the eye closure increases in the presence of phase noise (the eye is about 60% open for the case considered).

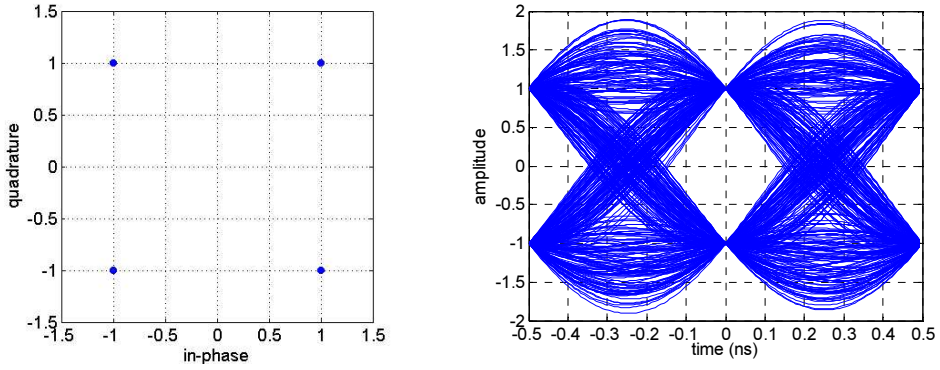

(a) No phase noise

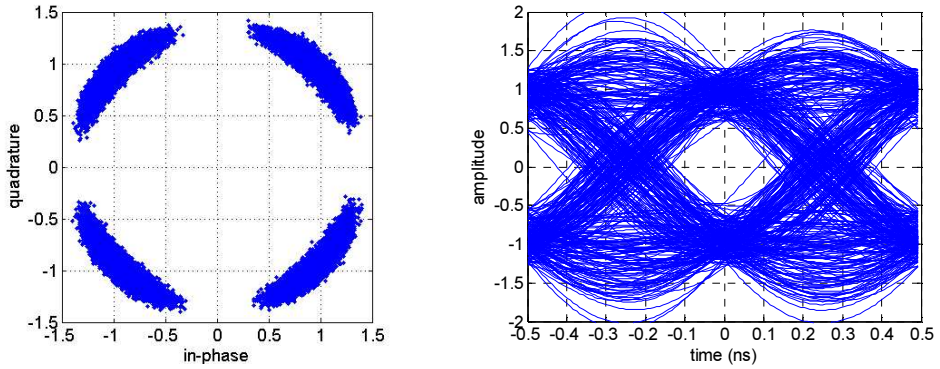

(b) Phase noise power level of -85 dBc/Hz

Figure 14 Scatter plots and eye diagrams for QPSK with no channel noise.

Figure 15 shows the scatter plots and eyediagrams of the demodulated QPSK signal.in the presence of both phase noise and channel noise. The plots shown in Figure 15 (a) have a channel noise of $E_b/N_0 = 15dB$ with no phase noise and those in Figure 15 (b) have both channel noise of $E_b/N_0 = 15dB$ and a phase noise level of -85dBc/Hz. We see that the eye is even more closed in the presence of both phase noise noise and channel noise. The Scatter plot constellation also spreads to cross the decision regions.

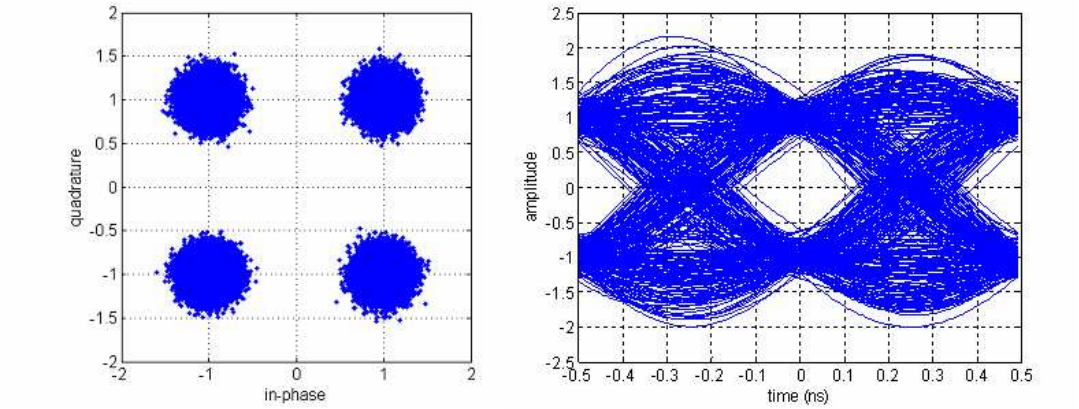

(a) Channel noise of $E_b/N_0 = 15dB$ with no phase noise

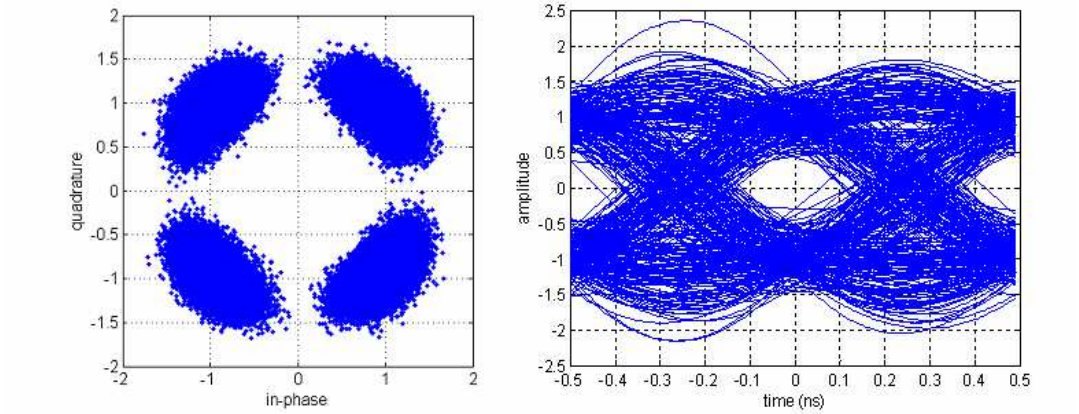

(b) Channel noise of $E_b/N_0 = 15dB$ and phase noise of power level -85dBc/Hz

Figure 15 Scatter plots and eye diagrams for QPSK with channel noise.

2.5.5 BER performance of BPSK with a costas loop at the receiver

One very common approach for carrier synchronization is to use a phase-locked loop (PLL) [2], [5], [9], [16], [20] demodulator. At the gigahertz frequency range, we suspect that any standard PLL will not be able to track random phase noise properly considering the relatively low response of the inherent low pass filter. Hence we also consider the BER performance of BPSK with a costas loop at the receiver in the presence of phase noise.

Carrier recovery (sometimes referred to as phase referencing) is the operation of extracting a phase coherent reference carrier from an observed noisy received carrier. When the received carrier is phase modulated such as BPSK (Binary Phase Shift Keying) or QPSK (Quadrature Phase Shift Keying), there is no direct carrier component to be tracked, and carrier recovery can not be obtained via a standard phase locked loop.

Instead a modified system must be used, which must first use a non-linearity to eliminate (wipe-off) the modulation while creating a carrier component having a phase variation proportional to that of the received carrier. Subsequent tracking of this residual carrier component then generates the desired carrier reference. The Costas, or quadrature, loop [2], [5], [7] is a common method for achieving this carrier recovery.

The classical Costas loop that is suitable for BPSK/QPSK demodulation is shown in Figure 16. The system involves two parallel tracking loops operating simultaneously from the same VCO (Voltage-Controlled Oscillator). The first loop, called the in-phase loop (or I arm), uses the VCO as in a PLL (Phase Locked Loop), and the second, called the quadrature loop (or Q arm) uses a 90 degree shifted VCO. The I and Q mixer outputs are filtered by matched low pass filters. The I and Q arm filter outputs are multiplied together and the product is scaled and filtered to produce the loop error used to control the VCO. The loop error should settle to a value when the loop is locked. A negative loop error decreases the VCO increment resulting in a lower VCO frequency, and similarly, a positive loop error increases the VCO increment resulting in a higher VCO frequency. The low pass filters in each arm must be wide enough to pass the data modulation without distortion. Thus when the loop is in the locked condition, the output of the I arm filter is the required demodulated base band signal.

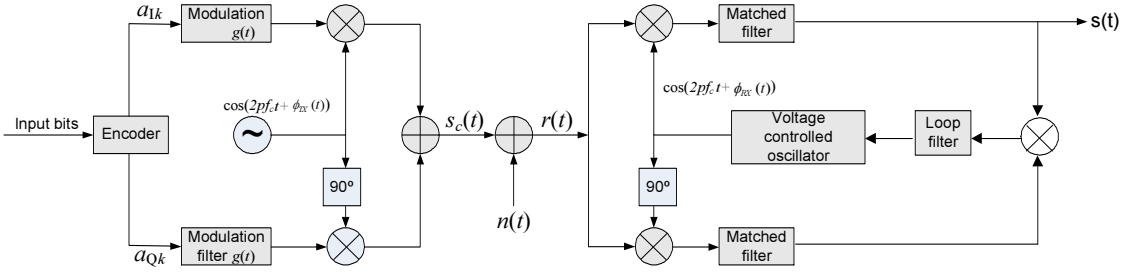

Figure 16 Costas receiver for BPSK demodulation

Figure 17 shows the bit error rate performance of BPSK using Costas receiver in the presence of phase noise. The simulation use a symbol interval of 0.5ns (or equivalently a data rate of 2Gbps) and a roll-off factor of 0.25 for the square-root raised-cosine pulse.

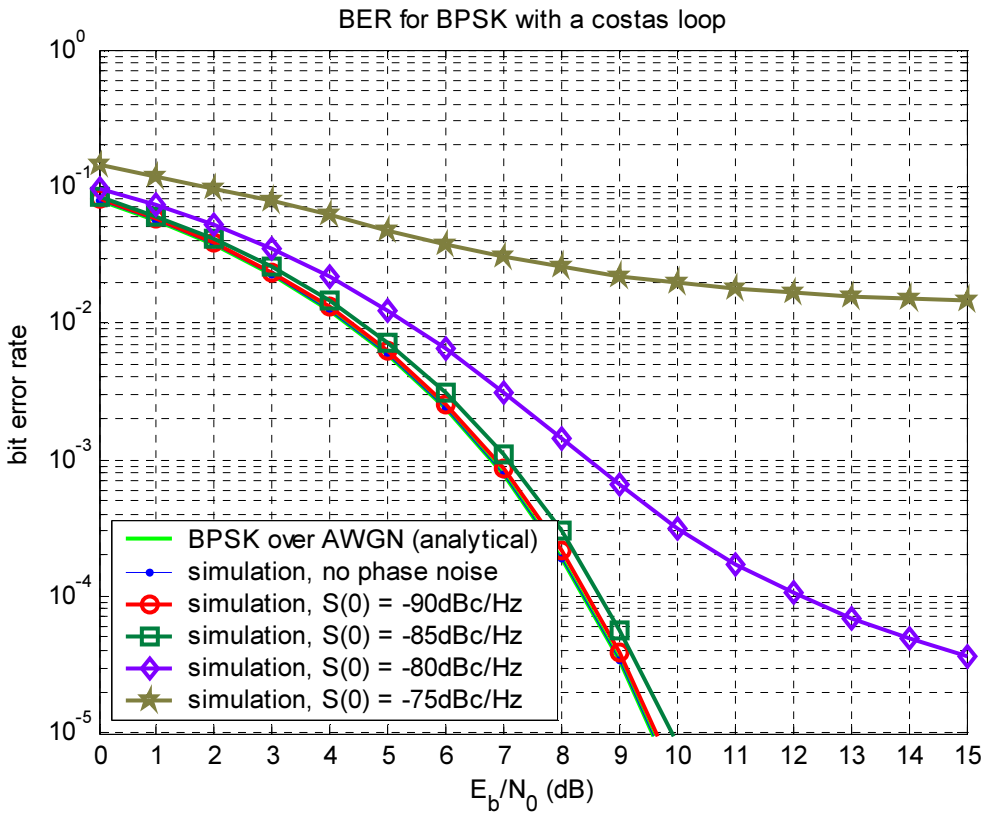

Figure 17 BER performance of costas loop in the presence of phase noise

One hundred packets of size 2kB (about 1.6×10^{6} bits) are transmitted. Four levels of phase noise power are considered. The carrier frequency is taken to be 3GHz. From Figure 17, we see that as the phase noise power level increases, the bit error rate increases sharply. More specifically, we can infer from Figure 17 that the costas loop locks when the phase noise is -90dBc/Hz and -85dBc/Hz. But when the phase noise is increased above -80dBc/Hz, the costas loop is not efficient in tracking the carrier which can be seen from the way the BER curve lifts upwards.

CHAPTER 3

PROPOSED MODULATION SCHEME

3.1 Introduction

The key idea here in reducing the effect of phase noise is that if we add a low power pilot to the transmitted signal and are able to recover the pilot signal at the receiver along with the phase noise information, then we can use the extracted pilot as a local oscillator which is automatically synchronized to the input signal, thus getting rid of the effect of the phase noise. An important constraint here is that there should be no signal information where the pilot is inserted, i.e., the power spectral density of the transmitted signal is zero at the pilot frequency. This can be easily implemented through proper coding schemes [4],[7],[14]. Meanwhile we want to achieve the maximum signaling rate in a given bandwidth, i.e., a signaling rate equal to the Nyquist rate of $2W$ symbols per second in a channel of bandwidth W hertz. This can be accomplished by adding inter-symbol interference (ISI) to the transmitted signal in a controlled manner [4],[7],[14]. This leads to our proposed *dual-rail bipolar* coding.

Figure 18 shows the block diagram of the complete system employing the pulse-amplitude-modulation (PAM) with a dual-rail bipolar signaling.

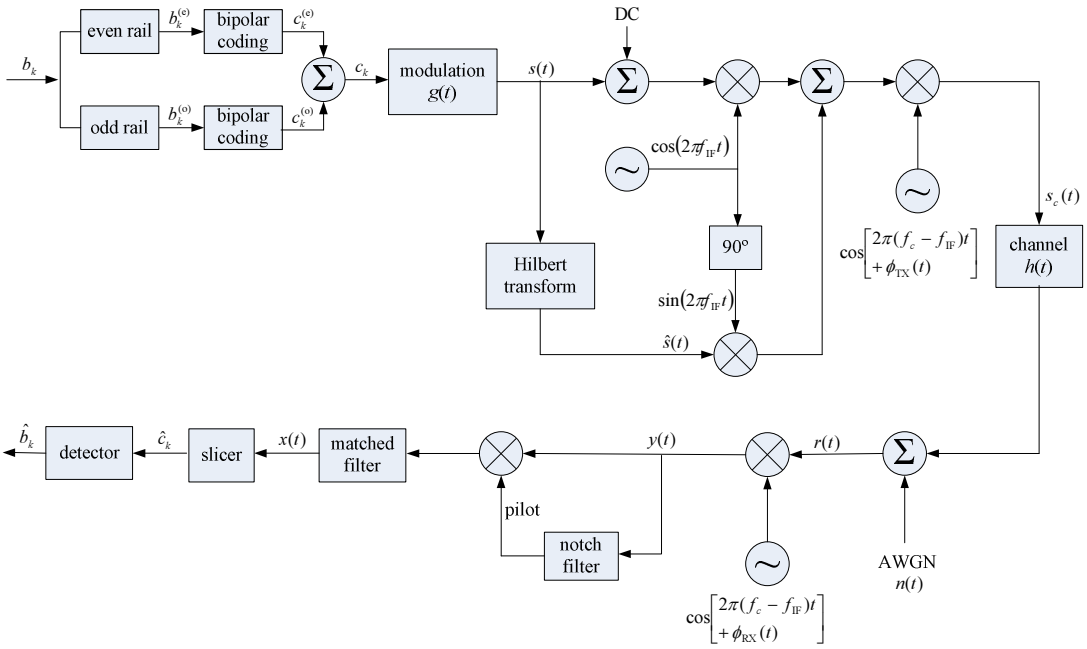

Figure 18 System block diagram for dual-rail bipolar scheme.

The important functions carried out in the block diagram of Figure 18 are discussed in next several sections.

3.2 Dual-Rail Bipolar Coding

Let $\{b_k\}$ ($b_k = 0$ or 1) be the original input binary sequence with bit rate R_b (correspondingly the bit interval is $T_\mathrm{b} = 1/R_\mathrm{b}$). This sequence is split into two rails defined as follows:

$$b_k^{(\mathrm{o})} = \begin{cases} b_k & \text{if } k \text{ is odd} \\ 0 & \text{if } k \text{ is even} \end{cases} \quad \text{and} \quad b_k^{(\mathrm{e})} = \begin{cases} 0 & \text{if } k \text{ is odd} \\ b_k & \text{if } k \text{ is even} \end{cases}, \tag{20}$$

where the superscripts 'o' and 'e' denote odd and even, respectively. Each rail is modulated by mapping a 1 into either a positive pulse or a negative pulse such that consecutive 1's are represented by pulses with alternating polarity, while a zero is represented by the absence of a pulse, i.e.,

$$s^{(\mathrm{m})}(t) = \sum_k c_k^{(\mathrm{m})} g(t - kT_\mathrm{b}), \tag{21}$$

where the superscript 'm' = 'o' or 'e', $g(t)$ is a given baseband pulse (e.g., the square-root raised-cosine pulse as described in the previous section), and

$$c_k^{(\mathrm{m})} = \begin{cases} \pm 1 & \text{if } b_k^{(\mathrm{m})} = 1 \\ 0 & \text{if } b_k^{(\mathrm{m})} = 0 \end{cases} \tag{22}$$

The baseband dual-rail bipolar signal is simply the sum of the odd and the even rails:

$$s(t) = s^{(\mathrm{o})}(t) + s^{(\mathrm{e})}(t) = \sum_k \left(c_k^{(\mathrm{o})} + c_k^{(e)}\right) g(t - kT_b), \tag{23}$$

where the second equality explains why in Figure 18 the modulation pulse $g(t)$ is taken out after the summation block. Figure 19 illustrates this scheme through a simple example. Note that a rectangular pulse instead of the actual baseband pulse is drawn for illustrative purpose.

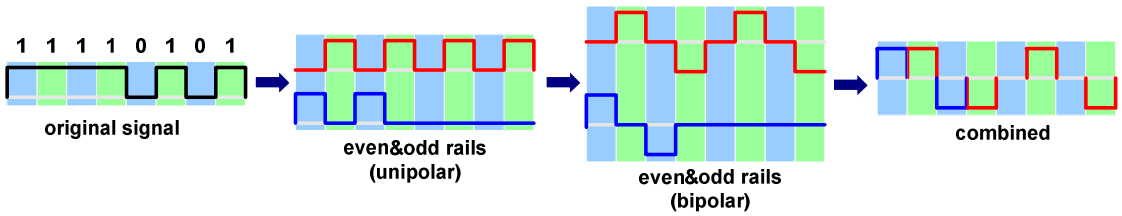

Figure 19 The dual-rail bipolar signaling scheme (illustrated through an example).

The transmitted RF signal (an SSB modulated signal) can be written as

$$s_{\mathrm{RF}}(t) = s(t)\cos\left[2\pi f_{\mathrm{c}} t + \phi_{\mathrm{TX}}(t)\right] + \hat{s}(t)\sin\left[2\pi f_{\mathrm{c}} t + \phi_{\mathrm{TX}}(t)\right], \tag{24}$$

where f_{c} is the carrier frequency (e.g., 60GHz), $\phi_{\mathrm{TX}}(t)$ is the phase noise, and $\hat{s}(t)$ is the Hilbert transform of the baseband signal $s(t)$. In addition to the selected sideband, two low-power pilot carriers are also transmitted to enable fast carrier and clock recovery. Note that only one pilot (corresponding to the DC component in Figure 18) is shown in the block diagram.

It is noted that a very important feature of the dual-rail bipolar modulation scheme is that the power of the baseband signal $s(t)$ is concentrated in the central region of $1/4T_{\mathrm{b}}$ while producing zeros at DC and $1/2T_{\mathrm{b}}$ so that the system utilizes approximately the minimum bandwidth of $1/2T_{\mathrm{b}}$. The zeros at DC and $1/2T_{\mathrm{b}}$ allow relatively easy extraction of the pilot carriers at the receiver. It can be shown that the power spectral density of $s(t)$ is given by [4]

$$S(f) = \frac{1}{T_{\mathrm{b}}} |G(f)|^2 \, M(f), \tag{25}$$

where $G(f)$ is the Fourier transform of the baseband pulse $g(t)$ and $M(f)$ is the spectral density shaping function for the dual-rail bipolar coding and is given by [4]

$$M(f) = 4p(1-p)\sin^2\left(2\pi T_{\mathrm{b}} f\right), \tag{26}$$

where p is the probability that $b_k = 1$. In the case when 1's and 0's are equiprobable, i.e., $p = 0.5$, $M(f) = \sin^2\left(2\pi T_{\mathrm{b}} f\right)$. Figure 20 shows an example of $S(f)$ along with plots of $M(f)$ and $|G(f)|$. In this example, the input data bit rate is 2Gbps (the bit interval $T_{\mathrm{b}} = 0.5$ ns and the transmission bandwidth is 1 GHz) and a square-root raised-cosine pulse with a roll-off factor of 0.25 is used.

It is also interesting to note that the bipolar modulation scheme provides some degree of error-detection capability in that an error in any bit will cause a *bipolar violation*, i.e., the reception of two or more consecutive 1's with the same polarity [4].

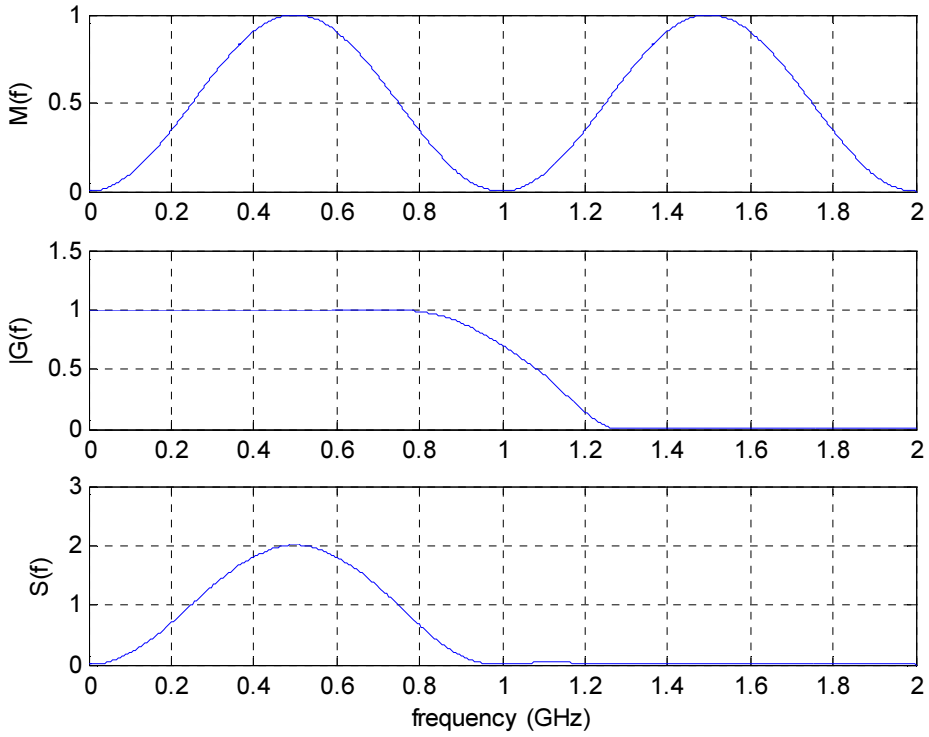

Figure 20 Power spectral density of the baseband dual-rail bipolar signal.

3.3 Narrow Band Pass Filter

The narrow band pass filter (NBPF) is one of the important components at the receiver side and needs careful design [19], [48]. It is used to recover the pilot along with the phase noise information which is then used as the local oscillator to eliminate phase noise from the recovered signal. The bandwidth is chose according to the phase noise profile given in Figure 5 and is typically at the level of a few tens of megahertz. We will now go through the mathematical expressions involved in the transmission and reception process. Again let $\phi_{\mathrm{TX}}(t)$ and $\phi_{\mathrm{RX}}(t)$ represent the phase noise from the transmitter and the receiver, respectively. The SSB modulated RF signal according to Figure 18 is given by

$$s_c(t) = s(t)\cos\left[2\pi f_c t + \phi_{\mathrm{TX}}(t)\right] + \hat{s}(t)\sin\left[2\pi f_c t + \phi_{\mathrm{TX}}(t)\right] + A_{\mathrm{p}}\cos\left[2\pi f_c t + \phi_{\mathrm{TX}}(t)\right] \quad (27)$$

where the last term represents the pilot carrier. The received signal (in the absence of channel noise) after down-conversion (assuming perfect image rejection) can be shown to be

$$y(t) = s(t)\cos[2\pi f_{IF}t + \phi(t)] - \hat{s}(t)\sin[2\pi f_{IF}t + \phi(t)] + A_p \cos[2\pi f_{IF}t + \phi(t)] \quad (28)$$

where $\phi(t) = \phi_{\mathrm{TX}}(t) - \phi_{\mathrm{RX}}(t)$. A factor of 2 is omitted for simplicity. Recall that the signal is designed such that its power spectral density is zero at the pilot frequency. So the NBPF can capture the pilot along with the phase noise information, i.e., the last term in equation (28), reasonably well. Figure 21 show the pilot recovery and delay compensation part of the system

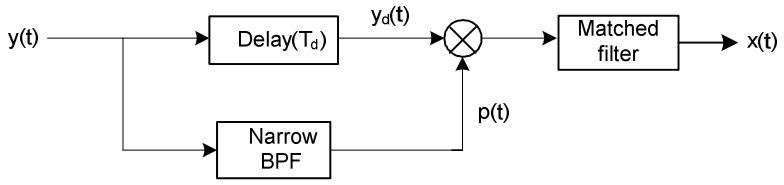

Figure 21 Pilot recovery and delay compensation

To analyse the effect the bandwidth of the narrow band pass filter on the phase noise performance, let us assume that the signal and the channel noise do not go through the narrow BPF (NBPF). Thus the input to the NBPF is

$$y_p(t) = A_p \cos[2\pi f_{IF}t + \phi(t)] \quad (29)$$

An ideal NBPF has the frequency response shown in Figure 22. The magnitude is unity and the phase is linear in the pass band, hence the group delay is constant, say T_d.

$$H_{NBPF}(f) = e^{-j2\pi(f-f_{IF})T_d}, \left|f_0 - BW\right| < f < \left|f_0 + BW\right| \quad (30)$$

where f_0 is the centre frequency and BW is the bandwidth. Expanding equation (24),

$$y_p(t) = A_p \cos(2\pi f_{IF}t)\cos\phi(t) - A_p \sin(2\pi f_{IF}t)\sin\phi(t) \quad (31)$$

Let $s_1(t) = A_p \cos\phi(t)$ and $s_2(t) = A_p \sin\phi(t)$. Let $S_1(f)$ and $S_2(f)$ be the Fourier transforms of $s_1(t)$ and $s_2(t)$. It is safe to assume that both $s_1(t)$ and $s_2(t)$ are narrow base band signals. For small $\phi(t)$, $\cos\phi(t) \cong 1$ and $\sin\phi(t) \cong \phi(t)$. Taking Fourier transform on both sides of equation (25) and just considering only the positive frequencies for the sake of simplicity,

$$Y_p(f) = (1/2)[S_1(f - f_{IF})] - (1/2j)[S_2(f - f_{IF})] \quad (32)$$

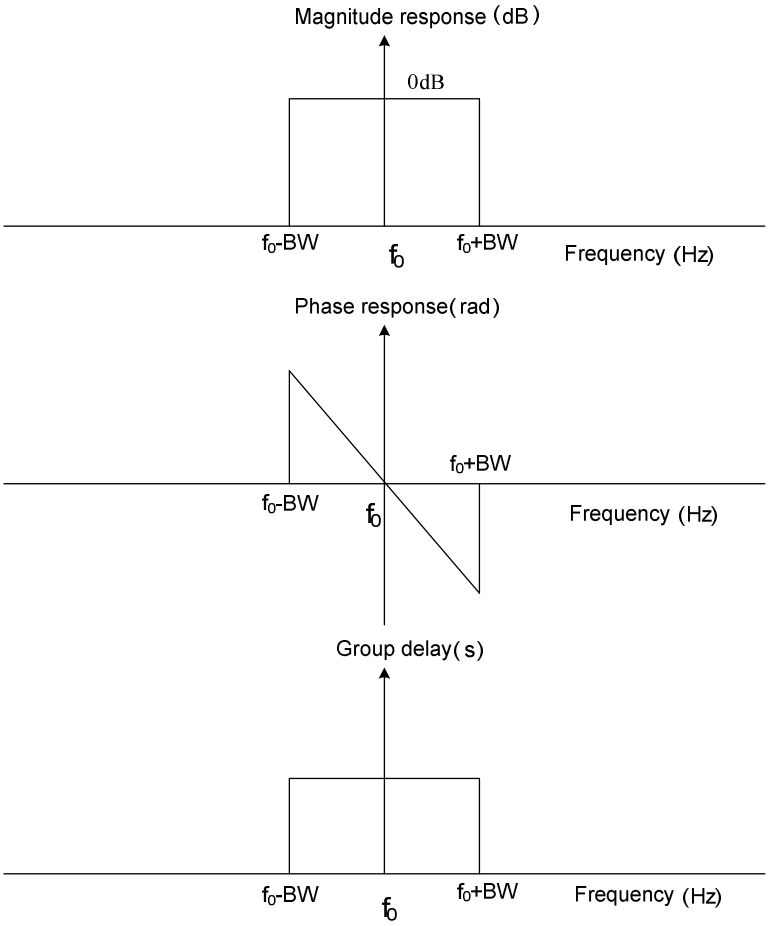

Figure 22 Ideal frequency response of the NBPF

The Fourier transform of the output of the NBPF is given by,

$$\begin{aligned} P(f) &= Y_P(f)H_{NBP}(f) \\ &= (1/2)[S_1(f-f_{IF})]e^{-j2\pi(f-f_{IF})T_d} - (1/2j)[S_2(f-f_{IF})]e^{-j2\pi(f-f_{IF})T_d} \\ &= (1/2)S_1'(f-f_{IF}) - (1/2j)S_2'(f-f_{IF}) \end{aligned} \tag{33}$$

where

$$S_1'(f) = S_1(f)e^{-j2\pi(f-f_{IF})T_d} \tag{34}$$

$$S_2'(f) = S_2(f)e^{-j2\pi(f-f_{IF})T_d} \tag{35}$$

Taking inverse Fourier transforms of the equations (34) and (35),

$$s_1'(t) = s_1(t-T_d) = A_p\cos[\phi(t-T_d)] \tag{36}$$

$$s_2'(t) = s_2(t-T_d) = A_p\sin[\phi(t-T_d)] \tag{37}$$

$$
\begin{aligned}
p(t) &= s_1'(t)\cos(2\pi f_{IF}t) - s_2'(t)\sin(2\pi f_{IF}t) \\
&= A_p\cos[\phi(t-T_d)]\cos(2\pi f_{IF}t) - A_p\sin[\phi(t-T_d)]\sin(2\pi f_{IF}t) \\
&= A_p\cos[2\pi f_{IF}t + \phi(t-T_d)]
\end{aligned}
\tag{38}
$$

Equation (38) gives the output of the NBPF. Note that the delay T_d occurs only in the phase noise term and not in the centre frequency of the NBPF. This is because the phase of the NBPF is zero at the centre frequency.

The following are the Elliptic NBPF design parameters:

a) Centre frequency 1.2GHz,

b) Pass band width 50MHz,

c) Pass band ripple 100mdB,

d) Stop band ratio 2.455,

e) Stop band width 122.7MHz and

f) Stop band attenuation 30dB

The third order elliptic band pass filter circuit designed with these parameters is shown in Figure 23.

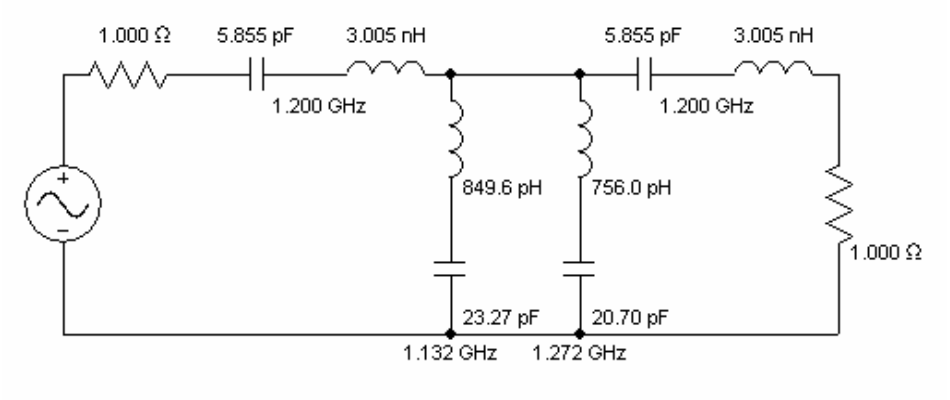

Figure 23 Elliptic NBPF circuit

The transfer function of the circuit in Figure 23 is,

$$
\frac{6.999e{+}07*S^5 + 8.012e{+}27*S^3 + 2.262e{+}47*S}{S^6 + 5.957e{+}08*S^5 + 1.708e{+}20*S^4 + 6.778e{+}28*S^3 + 9.71e{+}39*S^2 + 1.925e{+}48*S + 1.837e{+}59}
\tag{39}
$$

Figures 24 - 26 show the magnitude, phase and group delay responses of this filter respectively.

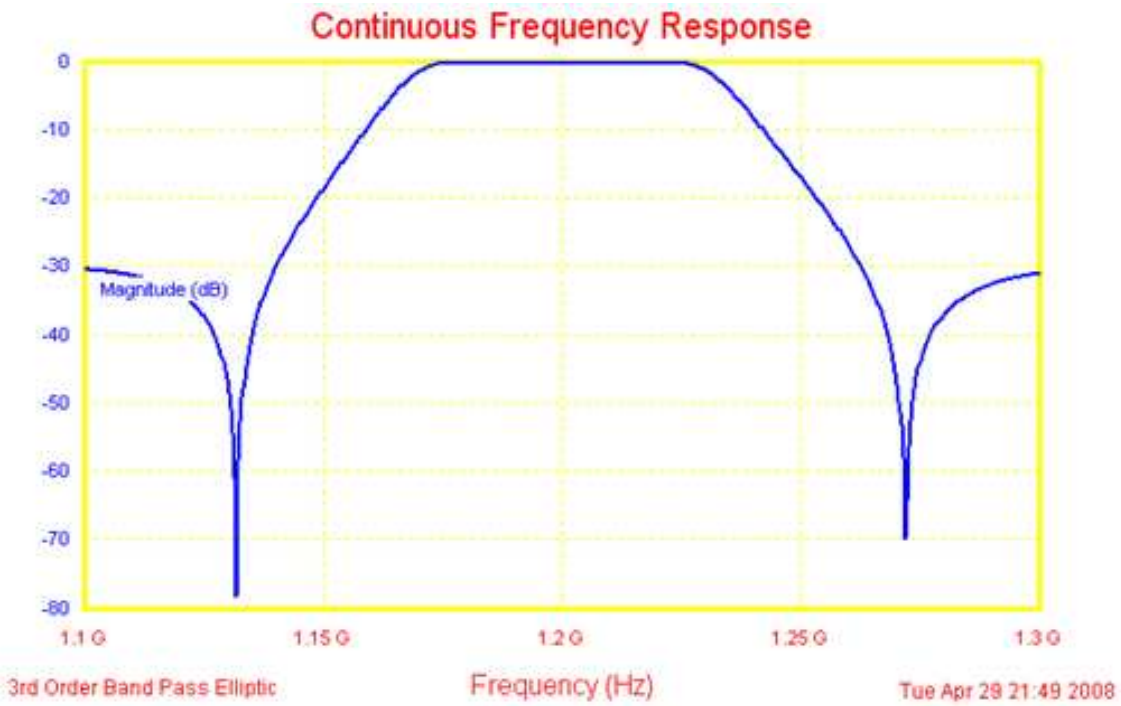

Figure 24 Magnitude response of the 3rd order elliptic NBPF

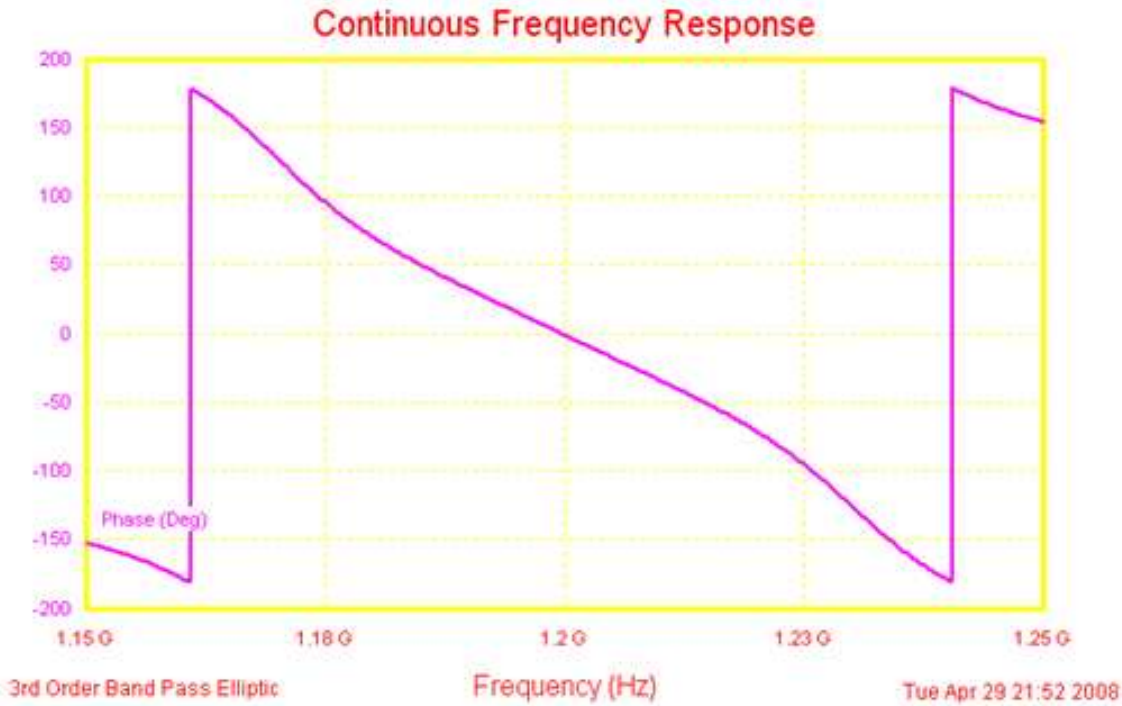

Figure 25 Phase response of the 3rd order elliptic NBPF

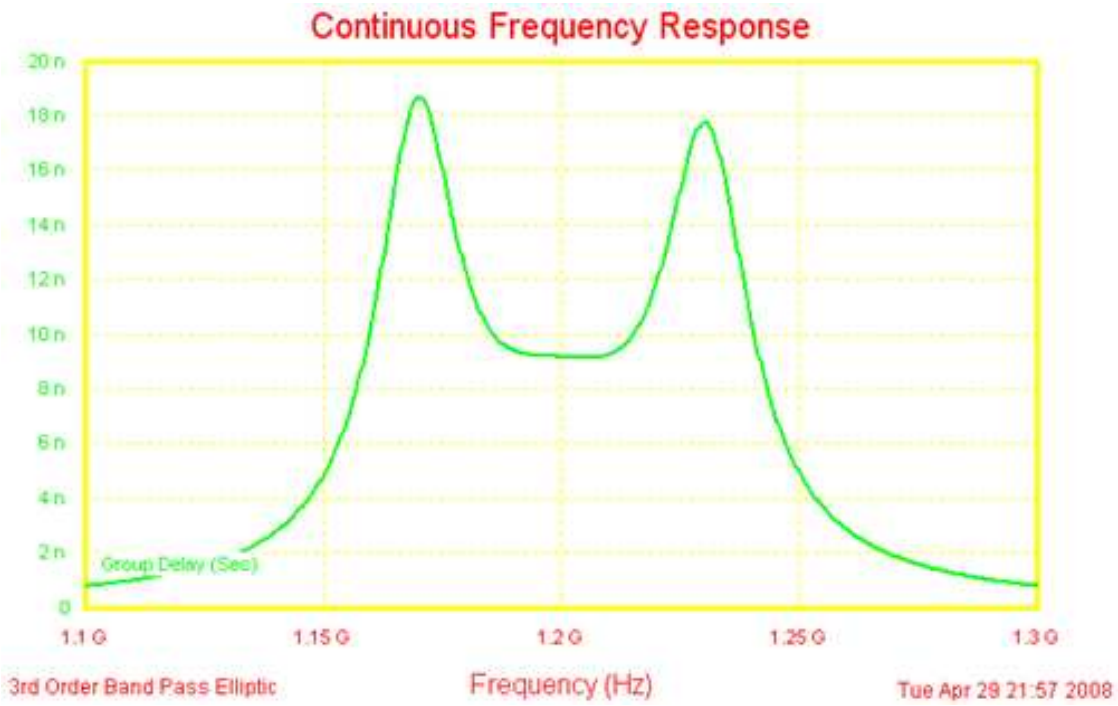

Figure 26 Group delay of the 3rd order elliptic NBPF

From Figure 25 note that the phase is linear in the desired band width centered at 1.2GHz and also exactly zero at the centre frequency 1.2GHz. Also note that the group delay in Figure 26 is constant over the desired bandwidth with a value of 9.25ns.

Without the use delay line, the output of the matched filter which is the low pass filtered version of the product $[p(t) \cdot y(t)]$ (product of equations (28) and (38)) is given by

$$x(t) = s(t)\cos[\phi(t) - \phi(t - T_d)] + \hat{s}(t)\sin[\phi(t) - \phi(t - T_d)] + A_p \cos[\phi(t) - \phi(t - T_d)] \quad (40)$$

We believe that the delay T_d may not have much effect in degrading the phase noise performance based on the following explanation.

The autocorrelation of the phase noise is calculated and plotted in Figure 27. For our system we need a delay line of 9.25ns. From Figures 27 and 28 we see that the autocorrelation for a delay of $T_d = 9.25ns$ is $R(9.25ns) = 0.95 \cong 1$ and hence $\phi(t) \cong \phi(t - T_d)$. Substituting this in equation (27) we get $x(t) \cong s(t) + A_p$ from which the desired base band signal $s(t)$ is obtained after passing through a slicer.

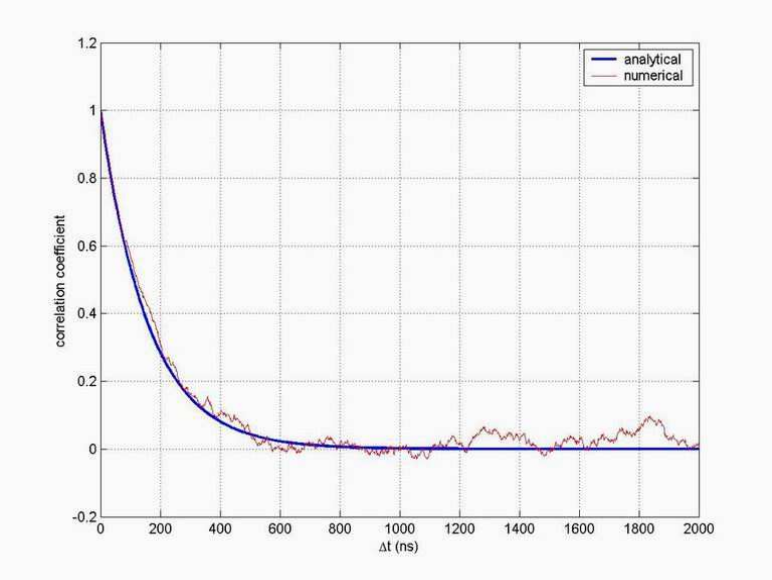

Figure 27 Autocorrelation of phase noise

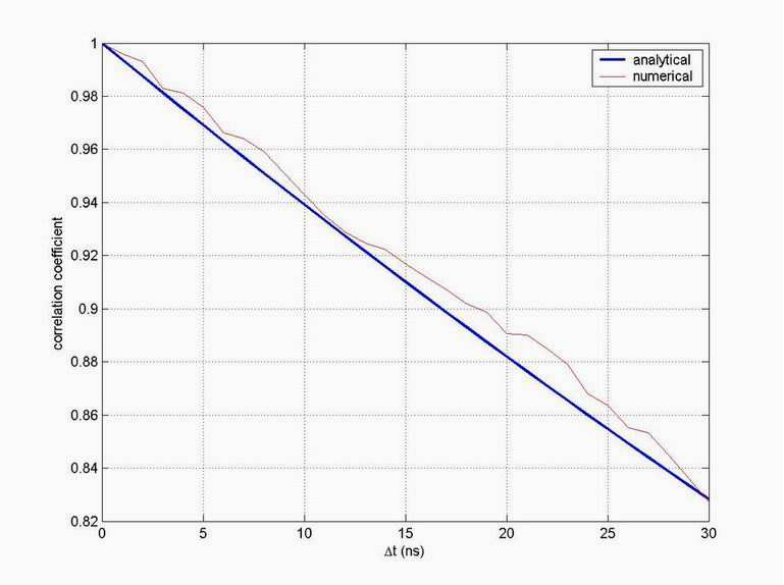

Figure 28 Zoomed-in view of Figure 27

Figure 29 shows the BER performance of the DRB scheme without a delay line. Now we need to compare the BER performance of this DRB scheme with some standard schemes. It makes sense to compare this scheme with the standard QPSK (without any compensation) since the spectral efficiency of this scheme is (2 Gbps/1.0 GHz = 2.0 bps/Hz) which is same as that of QPSK. Comparing Figure 29 and Figure 12, we can easily see that the BER performance of DRB is much better than the QPSK at high phase noise levels of -85dBc/Hz and above.

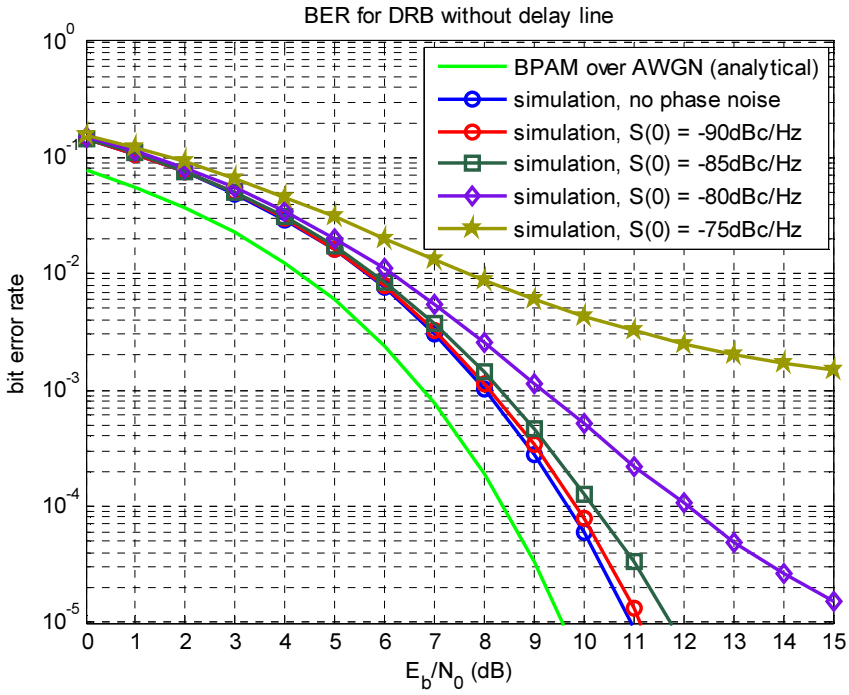

Figure 29 BER performance of DRB without a delay line

But the explanation based on autocorrelation of phase noise for omitting the delay line without degrading the phase noise performance is not so convincing since unlikely events may dominate error probability. Hence we also go on to analyze the delay line and its effect on phase noise performance.

Consider the output of an ideal delay line of T_d,

$$\begin{aligned} y_d(t) &= y(t-T_d) = s(t-T_d)\cos[2\pi f_{IF}(t-T_d)+\phi(t-T_d)] \\ &-\hat{s}(t-T_d)\sin[2\pi f_{IF}(t-T_d)+\phi(t-T_d)]+A_p\cos[2\pi f_{IF}(t-T_d)+\phi(t-T_d)] \end{aligned} \tag{41}$$

The output of the LPF following the mixer is then,

$$x(t) = s(t-T_d)\cos[2\pi f_{IF}T_d]-\hat{s}(t-T_d)\sin[2\pi f_{IF}T_d]+A_p\cos[2\pi f_{IF}T_d] \tag{42}$$

where the last term is just a constant corresponding to the DC value that can be removed easily. Then,

$$x(t) = as_d(t)-\sqrt{1-a^2}\,\hat{s}_d(t) \tag{43}$$

where,

$$a = \cos[2\pi f_{IF}T_d] \tag{44}$$

$$s_d(t) = s(t-T_d) \tag{45}$$

Taking Fourier transform on both sides of Equation (43)

$$X(f) = aS_d(f) - \sqrt{1-a^2}\, j\,\mathrm{sgn}(f)\hat{S}_d(f) \tag{46}$$

$$S_d(f) = X(f)/[a - \sqrt{1-a^2}\, j\,\mathrm{sgn}(f)] = [a + \sqrt{1-a^2}\, j\,\mathrm{sgn}(f)]X(f) \tag{47}$$

Taking inverse Fourier transform of Equation (47), we get

$$s_d(t) = ax(t) + \sqrt{1-a^2}\,\hat{x}(t) \tag{48}$$

where‘ a ’depends only on the NBPF and is known.

Thus, a delayed version of the desired base band signal is obtained. From equation (48) we see that in addition to the delay line, we also need a Hilbert transform circuit to get back the original base band signal. In this thesis, for the purpose of simulation we will use only an ideal delay line and ideal Hilbert transform. But we will talk briefly about the design of delay line and Hilbert transform.

Figure 30 shows the BER performance of the DRB scheme with an ideal delay line of 9.25ns and and ideal Hilbert transform circuit at the receiver. From Figures 29 and 30, we can see that the BER performance is better with the delay line than the case without delay line.

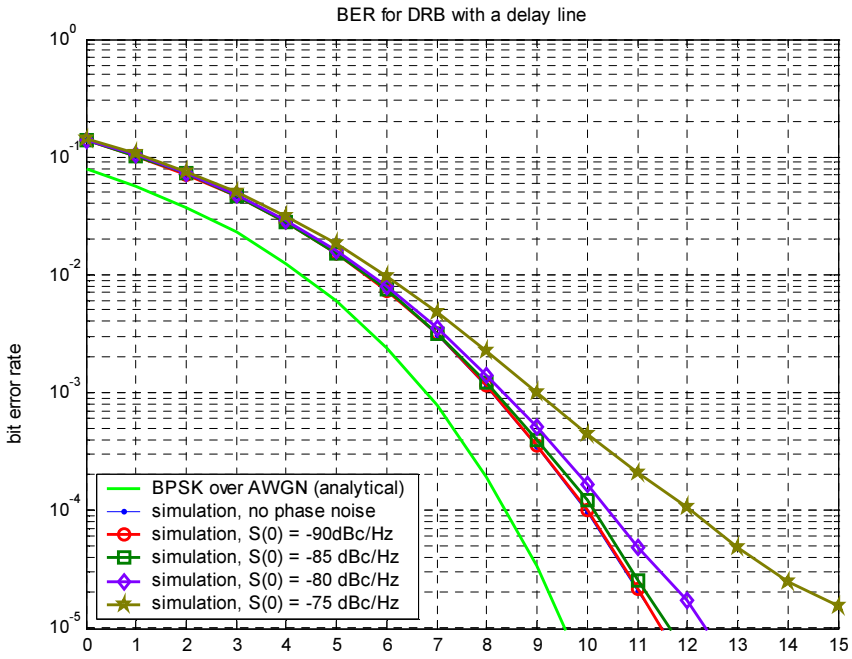

Figure 30 BER performance of DRB with a delay line

Now let us analyze how the bandwidth of the NBPF affects the phase noise performance. The bandwidth of the NBPF is chosen such that it is large enough to capture all the phase noise information and at the same time small enough not to capture much of the signal strength. For analysis purposes, let us now ignore the signal and just pass the pilot through the NBPF. We'll keep increasing the bandwidth so that much of the phase noise is captured and then plot the BER curves to see if there is any improvement in the BER performance. Figure 31 shows the instantaneous frequency variation with phase noise level of -80dBc/Hz. From Figure 31, we can see that most of the components of frequency variation are confined to approximately ± 40 MHz though actually much high frequency spikes may occur. This is reflected in Figure 32 which shows the effect of the NBPF bandwidth on the BER performance. We see that when bandwidth is above 80MHz, the BER is low since the filter captures most of the phase noise information whereas when the bandwidth decreases, the filter loses some phase noise information and the BER increases especially for the 40MHz case.

Similar explanations can be given to Figure 33 and Figure 34, for the phase noise level of -75dBc/Hz, except that here the frequency variation is higher and hence BER is higher than the previous case which suggest the bandwidth of the NBPF should be even higher which is not a feasible solution since it will start capturing the signal also. This is illustrated in Figures 35 – 38 when the signal is also present. We see that as we increase the bandwidth, the BER curves for different phase noise levels start converging towards each other. But we cannot choose the optimum bandwidth to be the one at which the BER curves converge because though the BER for high phase noise power reduces at this bandwidth, the BER for low phase noise power increases. Hence the best way to choose the bandwidth is to first find the phase noise level of the system and then choose the appropriate bandwidth from the given set of BER curves we have in Figures 35 - 38.

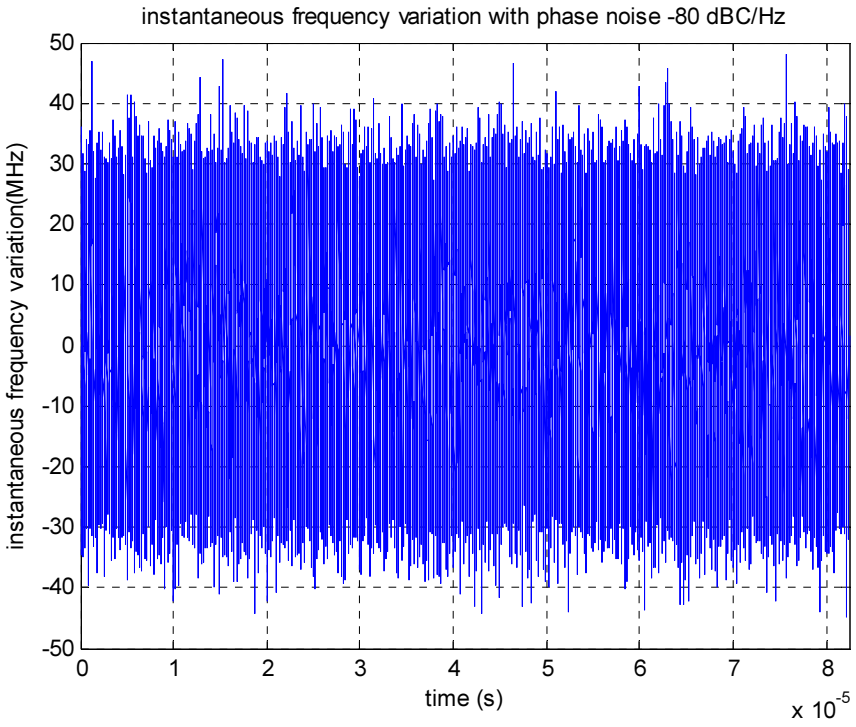

Figure 31 Instantaneous frequency variation with phase noise level -80 dBc/Hz

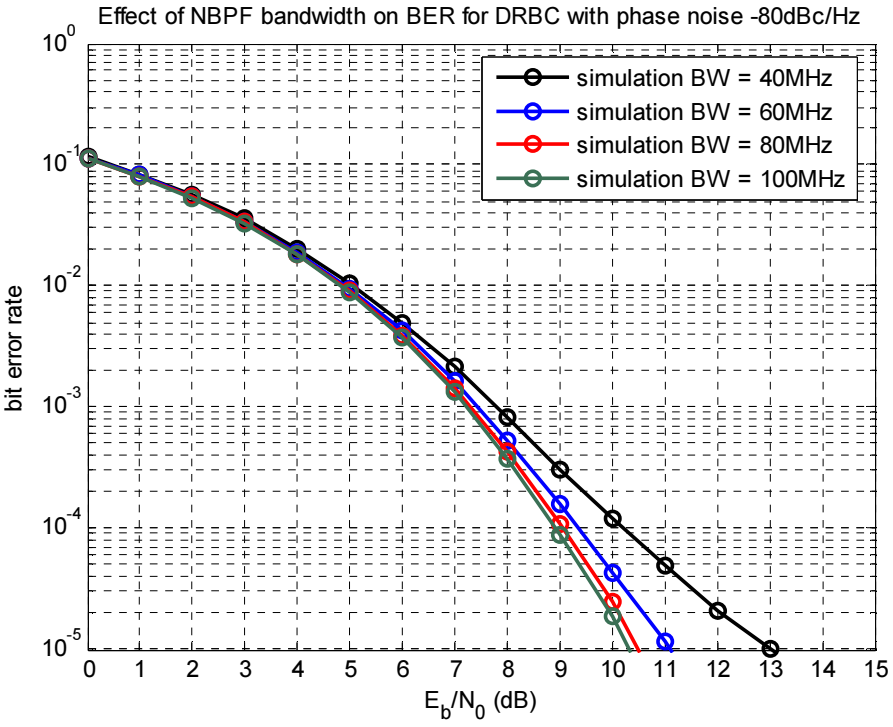

Figure 32 Effect of NBPF bandwidth on BER with phase noise level -80 dBc/Hz

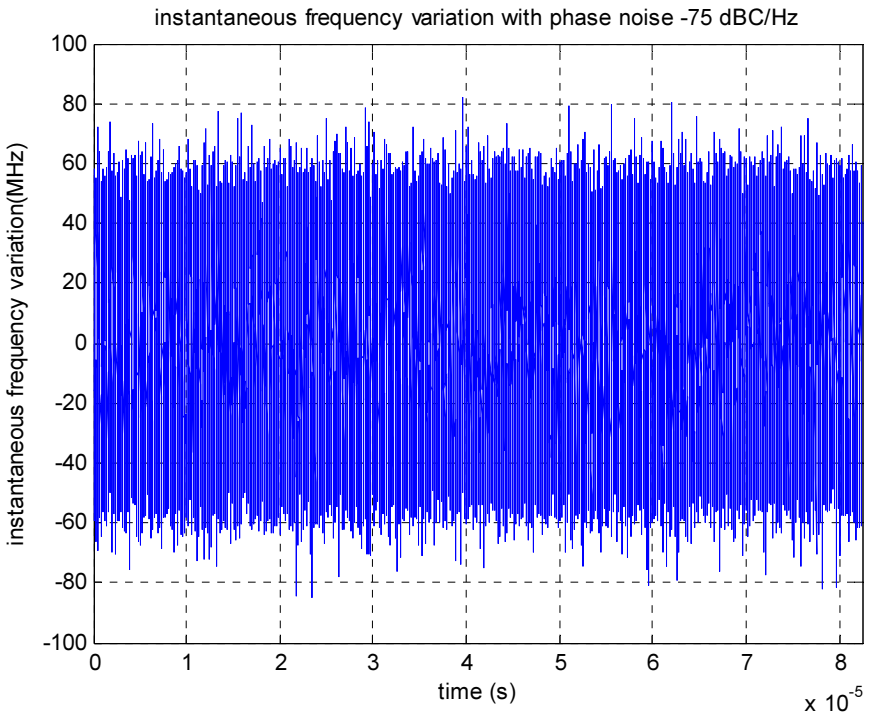

Figure 33 Instantaneous frequency variation with phase noise level -75 dBc/Hz

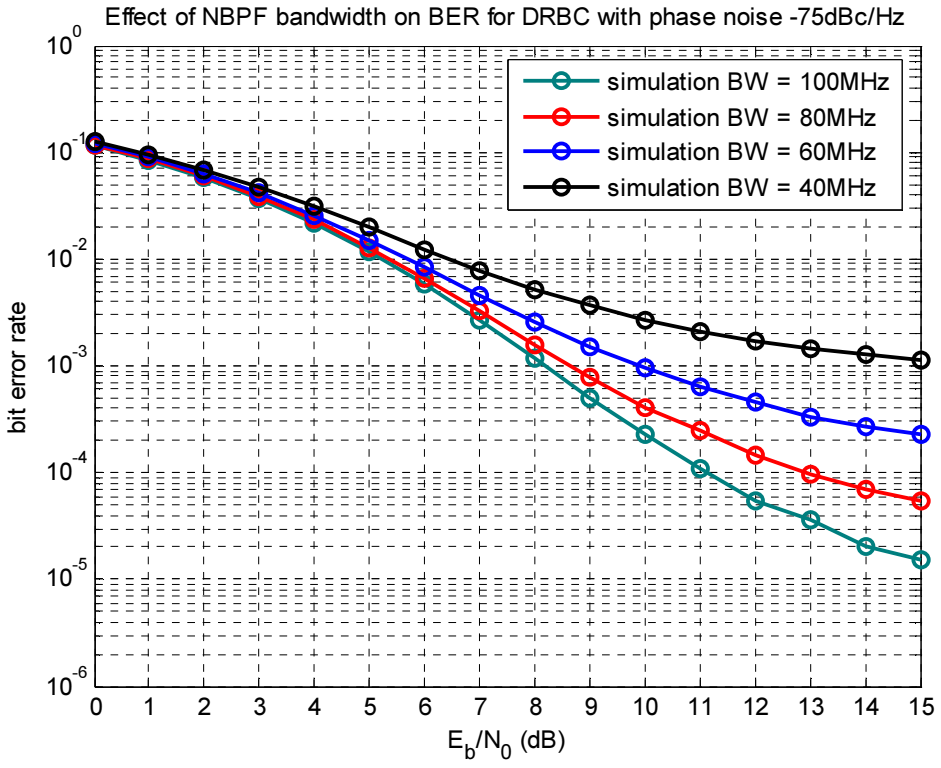

Figure 34 Effect of NBPF bandwidth on BER with phase noise level -75 dBc/Hz

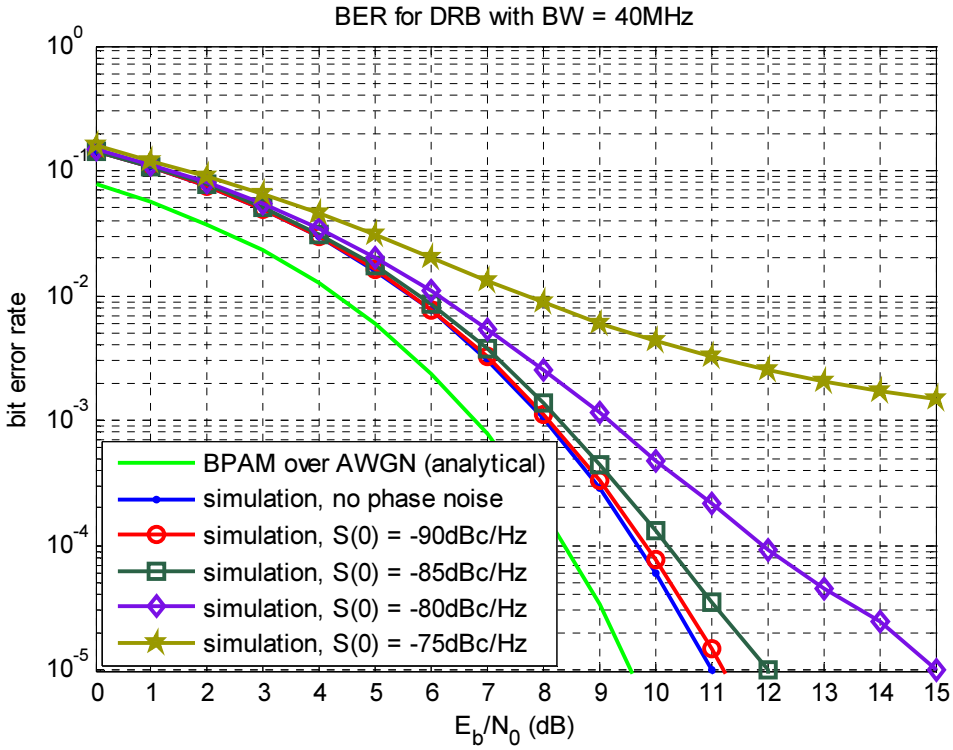

Figure 35 BER performance of DRB with NBPF bandwidth = 40MHz

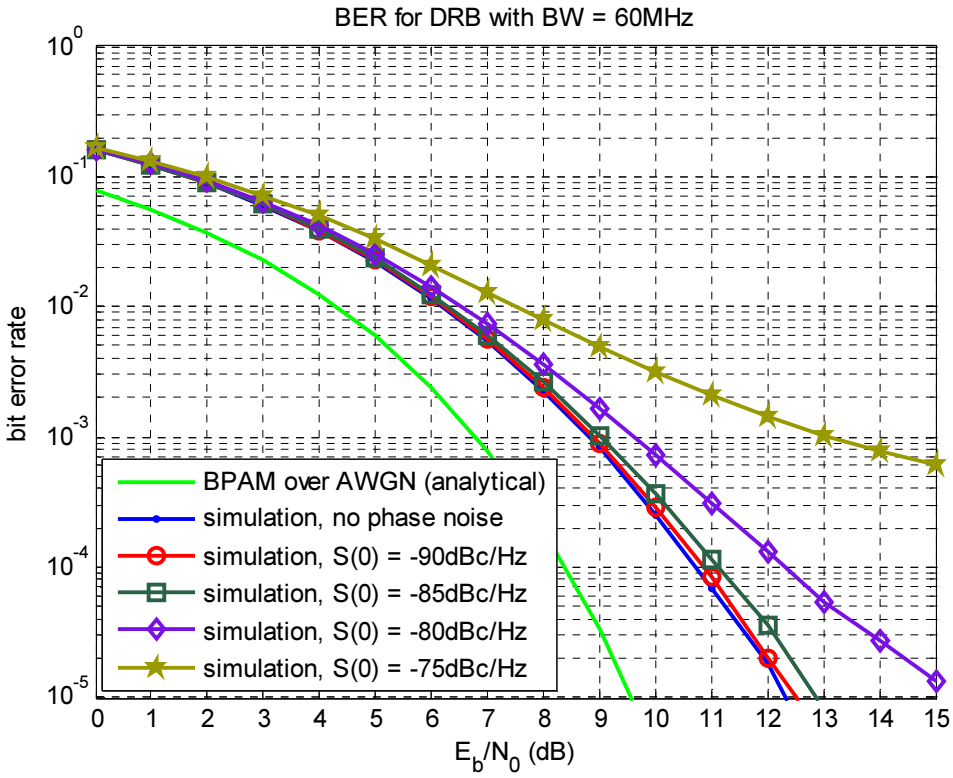

Figure 36 BER performance of DRB with NBPF bandwidth = 60MHz

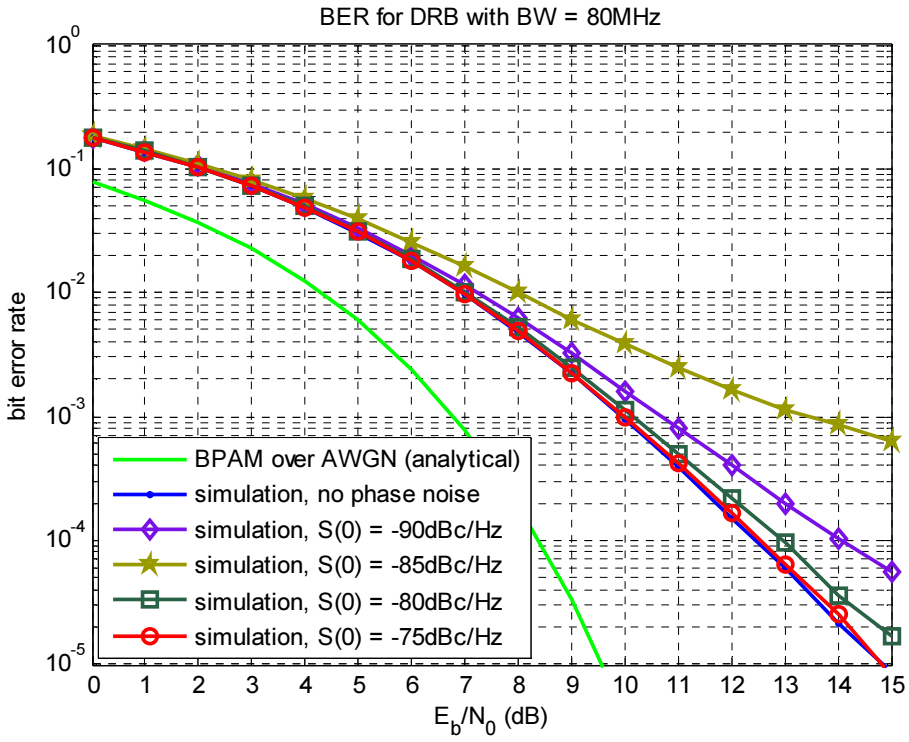

Figure 37 BER performance of DRB with NBPF bandwidth = 80MHz

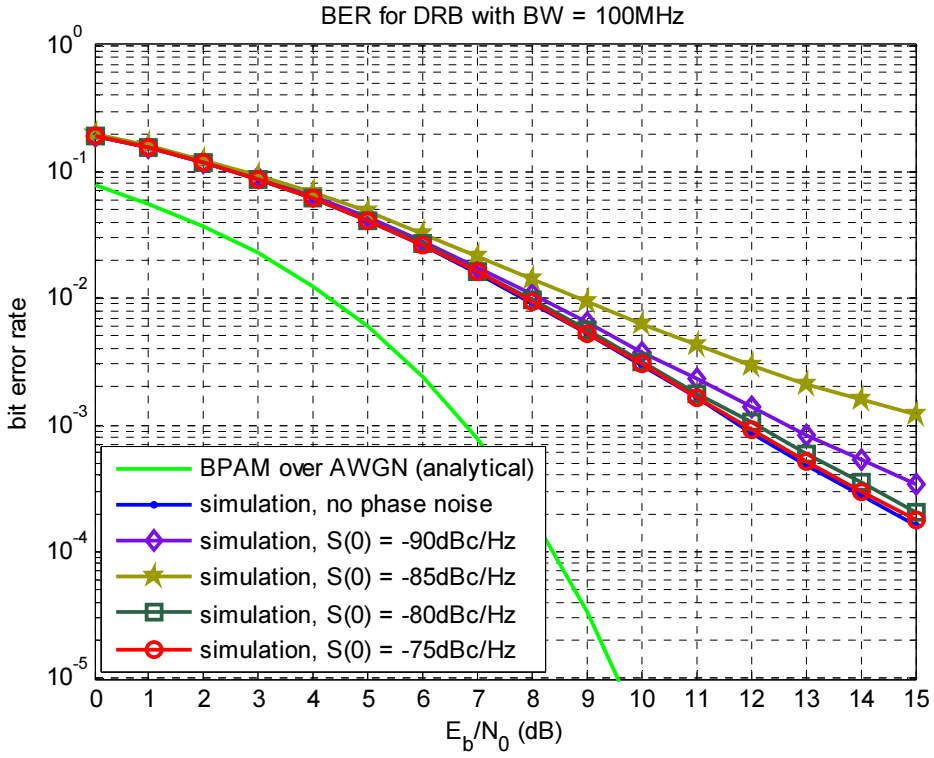

Figure 38 BER performance of DRB with NBPF bandwidth = 100MHz

3.4 Delay Line Design

As mentioned earlier, in this thesis, for the purpose of simulation we will use only an ideal delay line and ideal Hilbert transform. But we will talk briefly about the design of delay line in this section and Hilbert transform in the next section.

The system we designed needs a delay of 9.25ns. Let us consider the design [19] of delay line of $T_{gd} = 3.083ns$ over a bandwidth of $f_{gd} = 1.2Ghz$. So we will need 3 such delay lines. The required delay bandwidth factor is

$$TU_{req} = 2\pi f_{gd} T_{gd} = 2\pi(3.083ns)(1.2GHz) = 23.2 \tag{49}$$

From the tables of group delay characteristics for the linear phase constant ripple of 0.05 degree (1%), we select the low pass prototype such that its delay bandwidth factor $TU > TU_{req}$. Then the low pass transfer function can be transformed to all-pass transfer function by simply introducing zeros in the right half plane of the $j\omega$ axis corresponding to each pole. When a low pass to all pass transformation is made, the low pass delay is increased by a factor of exactly 2 because of the additional phase-shift contributions of the zeros. From the tables we find that for order n=10,

$$TU = \omega_u T_{gd}(DC) = 3(7.8) = 23.4 > TU_{req} \tag{50}$$

where $T_{gd}(DC)$ is the delay at DC. The delay scaling factor is given by

$$DSF = \frac{T_{gd}(DC)}{T_{gd}} = \frac{7.8}{3.083ns} \tag{51}$$

Hence we need to get the pole locations for the chosen filter and denormalize them as using the delay scaling factor as follows. For a real pole α_0, the scaling is done as,

$$\alpha_0^{'} = \alpha_0 DSF \tag{52}$$

and the transfer function is

$$T(s) = \frac{s - \alpha_0^{'}}{s + \alpha_0^{'}} \tag{53}$$

Figure 39 (a) shows the realization of this first order transfer function where

$$L = 2r / \alpha_0^{'} \tag{54}$$

$$C = 2/(\alpha_0^{'} R) \tag{55}$$

For complex poles $\alpha \pm j\beta$, the design parameters are,

$$\omega_r = DSF\sqrt{\alpha^2 + \beta^2} \tag{56}$$

$$Q = \frac{\omega_r}{2\alpha DSF} \tag{57}$$

The transfer function is

$$T(s) = \frac{s^2 - \frac{\omega_r}{Q}s + \omega_r^2}{s^2 + \frac{\omega_r}{Q}s + \omega_r^2} \tag{58}$$

Figure 39 (b) shows the realization of this second order transfer function where

$$L_a = 2R/\omega_r Q \tag{59}$$

$$L_b = QR/2\omega_r \tag{60}$$

$$C_a = Q/\omega_r R \tag{61}$$

$$C_b = 2Q/(\omega_r(Q^2 - 1)R \tag{62}$$

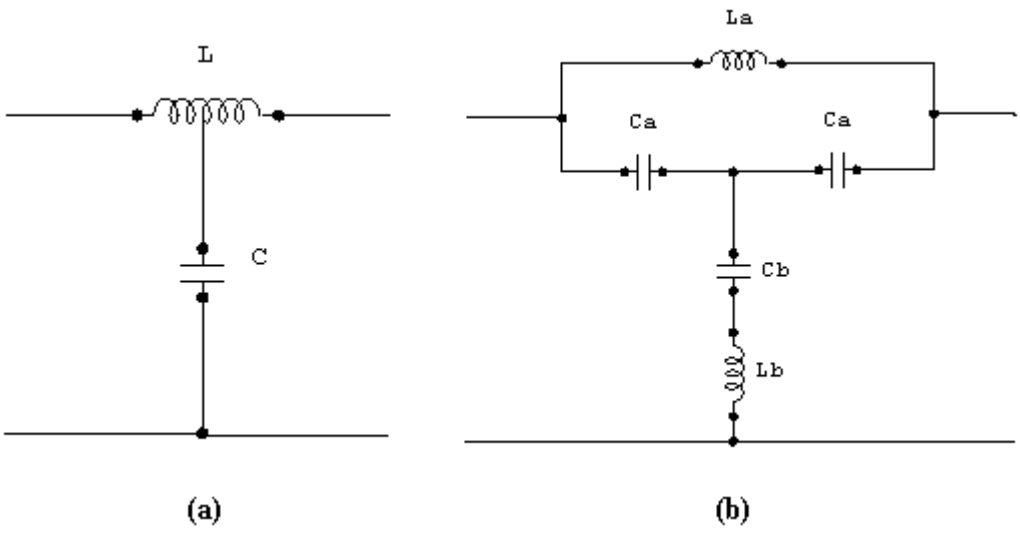

Figure 39 Constant resistance (a) first order and (b) second order circuits

Figure 40 shows the entire 10^{th} order circuit for the delay line which is a cascade of 5 stages of second order circuits.

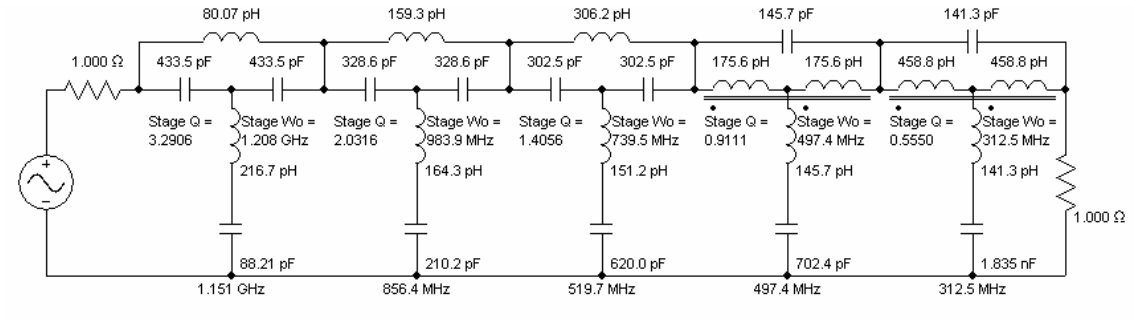

Figure 40 Tenth order delay line circuit

Figure 41 shows the group delay response of the delay line. We see that the group delay is a constant value of 3ns with a variation of only 0.01ns which is very negligible.

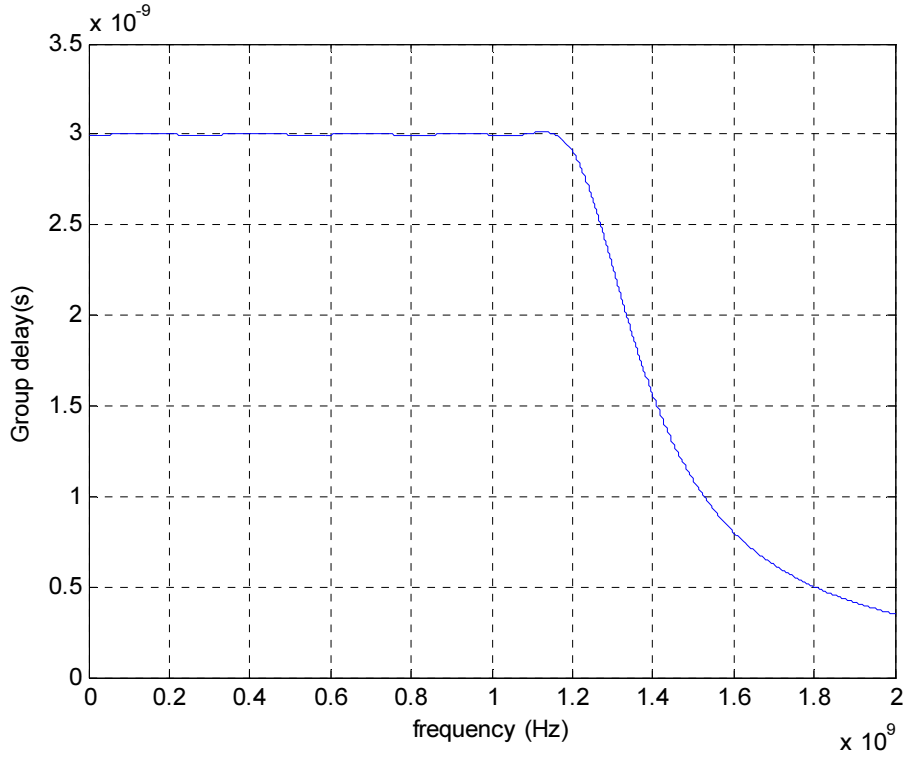

Figure 41 Group delay response of the delay line

Now let us see how the tolerance values of the components can affect the performance of the NBPF and the delay line. Let us allow a tolerance of 5% for inductors, 2% for capacitors and 1% for resistors. Figure 42 shows the Monte Carlo analysis for the group delay of the delay line with 250 runs and uniform distribution of the tolerance values. We see that there is a variation of less than 0.1ns up to 0.7GHz and

less than 0.3ns for frequencies above. This may have an effect on the BER performance of the overall system. But this problem can be easily resolved as follows. We know that our NBPF is a third order elliptic filter with 4 tank circuits. Our delay line also has 5 tank circuits. These tank circuits can be tuned for the desired frequencies using the simple tuning circuit shown in Figure 43. Hence though there is change in the magnitude and group delay responses of the filters due to the tolerance values of the components, they can be easily tuned to achieve the desired frequency response.

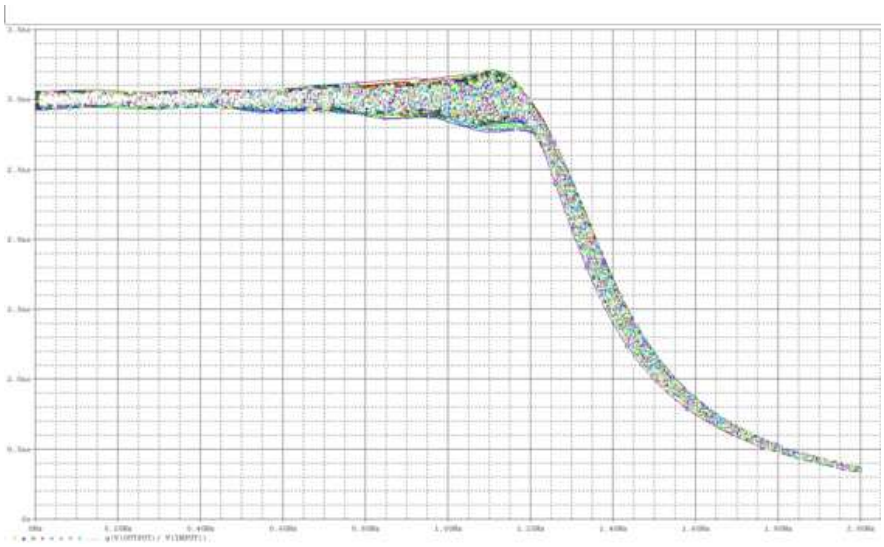

Figure 42 Monte Carlo analysis of the group delay of the delay line

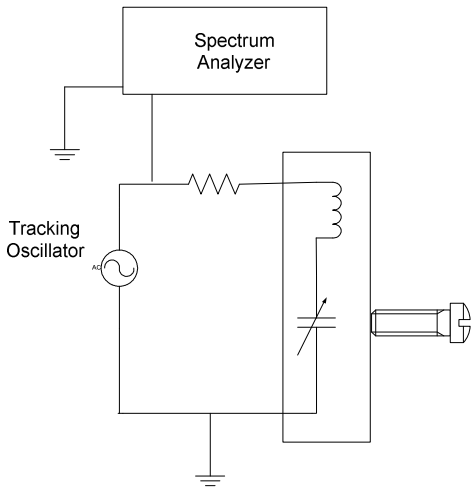

Figure 43 A simple tuning circuit for the NBPF and the delay line

.

The tank circuit shown in the Figure 43 can be tuned to the desired frequency by just turning the knob until we see the desired frequency in the spectrum analyzer. Say it approximately takes a minute for a person to tune this circuit. We have 4 such tank circuits in the narrow band pass elliptic filter. Hence it will approximately take 4 minutes for a person to tune the narrow band pass filter. Considering a wage rate of $15/hour, the tuning cost of the narrow band pass elliptic filter is (1/15) ($15) = $1. This is very cheap. Giga-hertz Trimmer capacitors are available for very low price.

In Figure 43, we have shown the tuning circuit as a discrete component. But since the ultimate goal would be designing a chip incorporating the frequency tuning capability, this can be done using varactors. [56] talks in detail about the characteristics of varactors. Since the junction capacitance of the varactors depend on the applied bias voltage, such a capacitor can be used to make electronically tuned circuits. The junction capacitance depends on the voltage bias as follows:

$$C_j = C_{j0} \Big/ (1 - V_F / \phi)^n \tag{63}$$

where C_{j0} is the incremental capacitance at zero bias, V_F is the amount of forward bias voltage applied across the junction, ϕ is the built-in potential and n is a parameter depending on the doping profile of the semiconductor used. [54] describes the process of fabricating tank circuits using CMOS technology and also the addition of varactors in the tank circuits so that tuning issues of the oscillator frequency can be addressed. [53] demonstrates a frequency domain tuning scheme for varactor TV tuners so that desired oscillator frequency is obtained. [52] demonstrates a varactor tuned low-cost 24GHz harmonic VCO. Electronic tuning ICs are available for very low price [56] of about $5.

3.5 Hilbert Transform Circuit design

The ideal Hilbert transform function is shown in the Figure 44. This is an all pass transfer function. The frequency response is given by,

$$H_{HT}(f) = \begin{cases} e^{j\pi/2}, f < 0 \\ e^{-j\pi/2}, f > 0 \end{cases} \tag{64}$$

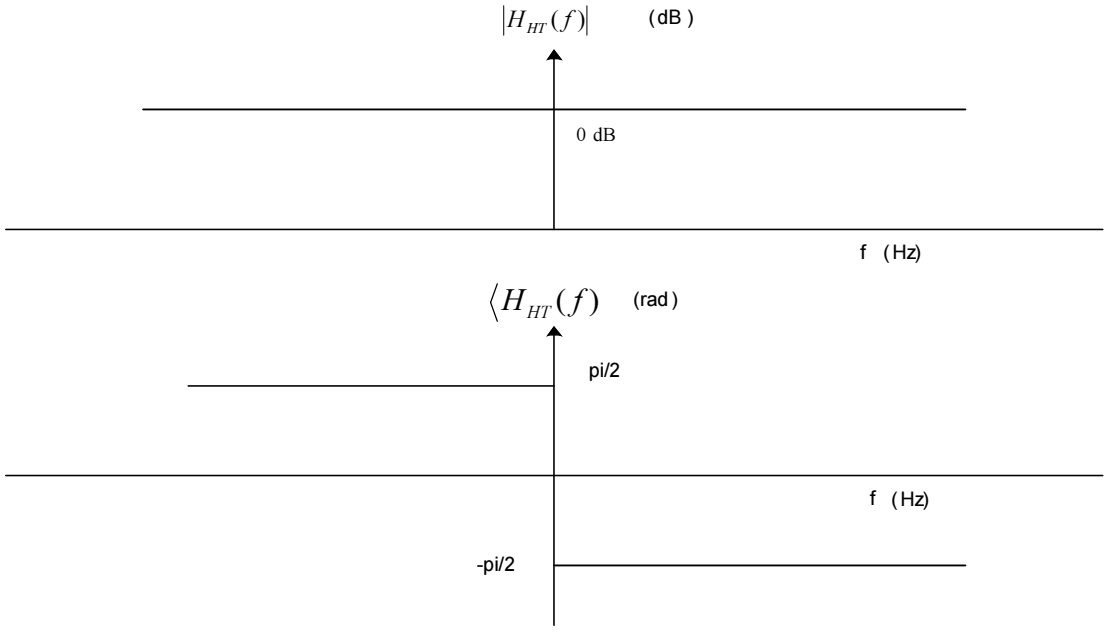

Figure 44 Frequency response of Hilbert transform

This all pass transfer function is just a 90-degree phase shift which can be designed [19], [48] as follows. . Wideband 90-degree phase shift networks have a single input port and two output ports, the output maintaining a constant phase difference of 90-degrees within a prescribed error $\Delta\phi$ over a wide band of frequencies. The general structure of 90-degree phase shift network consist of N and P networks as shown in Figure 45. The transfer function is of the form,

$$T(s) = \frac{(s-\alpha_1)(s-\alpha_1)\cdots\cdots(s-\alpha_{n/2})}{(s+\alpha_1)(s+\alpha_1)\cdots\cdots(s+\alpha_{n/2})} \tag{65}$$

Where $n/2$ is the order of the numerator and denominator polynomials and n is the total complexity of both networks.

Ideally, we need a 90-degree phase shift over the band 0-1GHz, which is very hard to design. The zero energy around DC and the relatively compact bandwidth allows DRB signals to be Hilbert transformed with relatively low complexity. It is calculated that about 99% of the signal power is within the band 100MHz – 900MHz. Hence, to make our job simpler, let us design a 90-degree phase shift only in this band where $f_L = 100MHz$ and $f_U = 900MHz$.

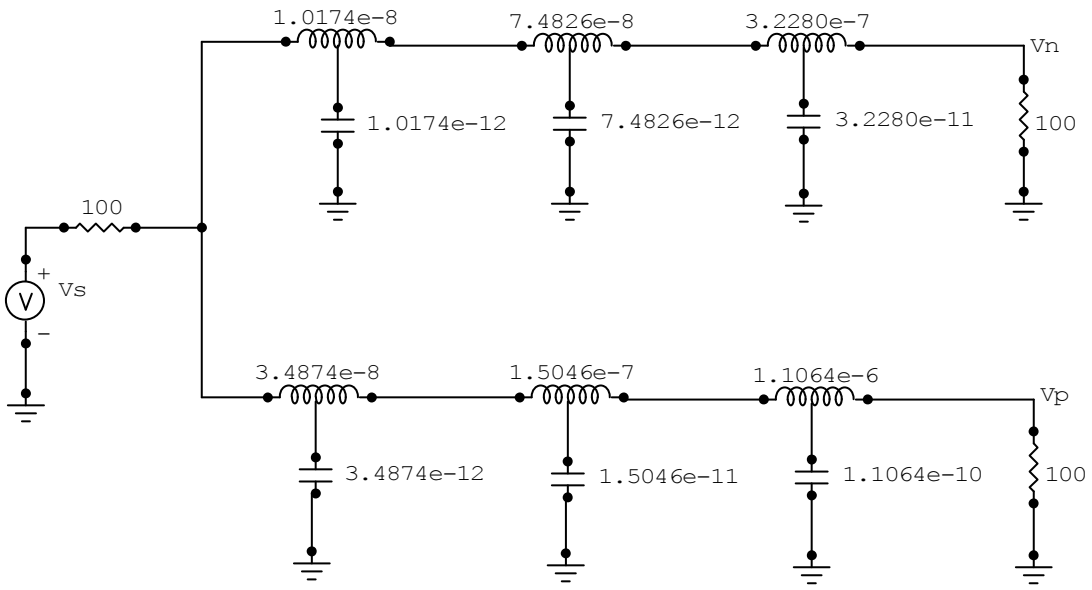

Figure 45 Wideband 90-degree phase shift network

The required bandwidth ratio is

$$(f_U / f_L)_{req} = 9 \tag{66}$$

From the Bedrosian [19] tables of pole-zero locations for 90-degree phase shift networks, we see that for order $n = 6$ and phase error $\Delta\phi = \pm 0.1$ degree,

$$f_U / f_L = 11.47 > (f_U / f_L)_{req} \tag{67}$$

which is suitable for our requirements. The frequency scaling factor is

$$FSF = 2\pi f_0 \tag{68}$$

where $f_0 = \sqrt{f_L f_U}$. Now the pole-zeros $\{\alpha\}$ from the Bedrosian tables are denormalised by multiplying them by the FSF to get the new pole-zeros $\{\alpha'\}$. The P and N networks can now be realized using passive first-order all pass constant resistance circuits shown in Figure 39 (a) in section 3.4. The designed 90-degree phase shift network is shown in Figure 45. The phase difference between the P and N networks is shown in Figure 46. We see that there is a constant phase difference of 90-degrees between the P and Q networks with a phase error of $\Delta\phi = \pm 0.1$ degree within the desired band of 100-900MHz.

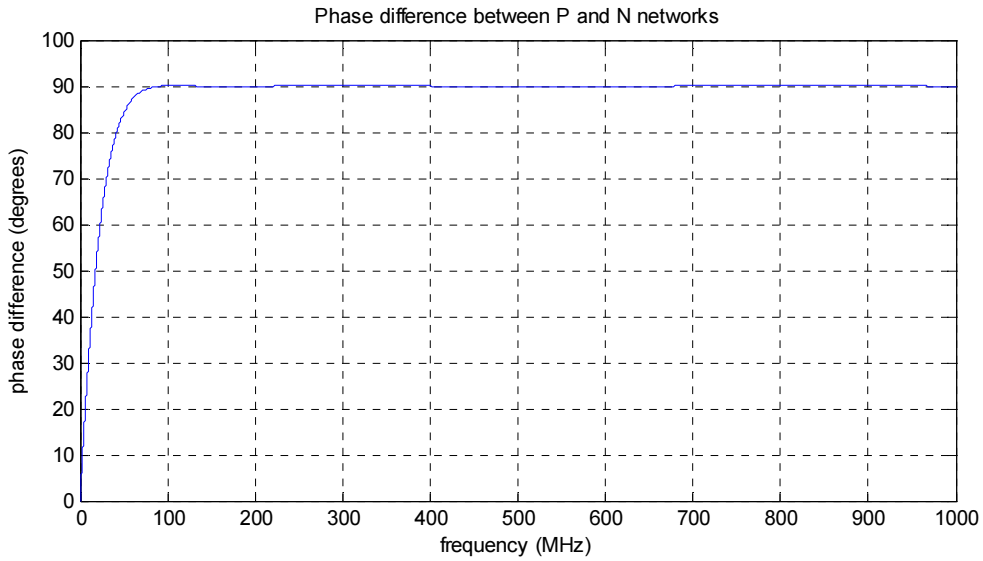

Figure 46 Phase difference between P and N networks

The group delay of the P network is the red curve shown in Figure 47. Since this is not constant over the desired bandwidth, we need a group delay equalizer for the P network. Figure 48 shows the designed group delay equalizer circuit for the P-network and the blue curve in Figure 47 shows the group delay after equalization which has a very small variation of 0.05ns.

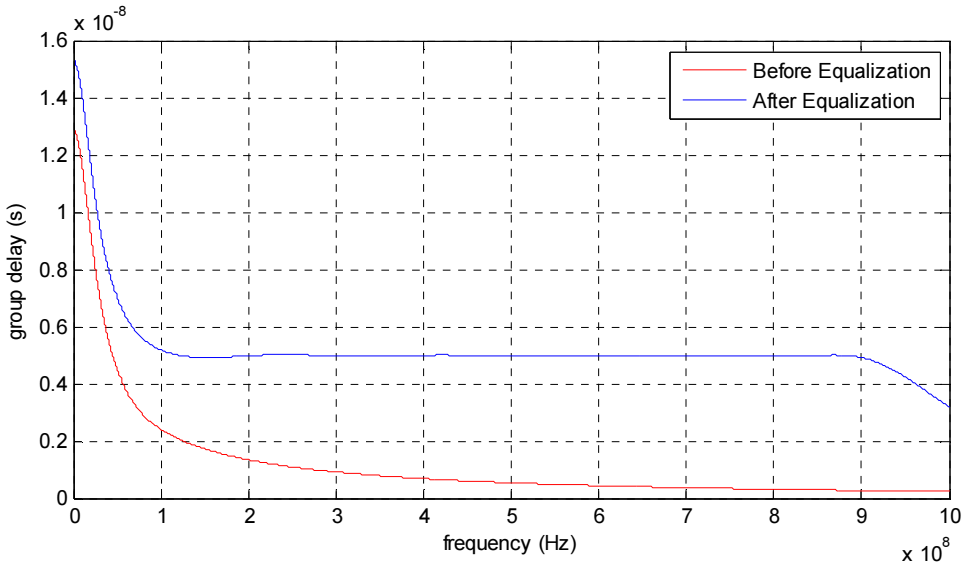

Figure 47 Group delay equalization of the P-network

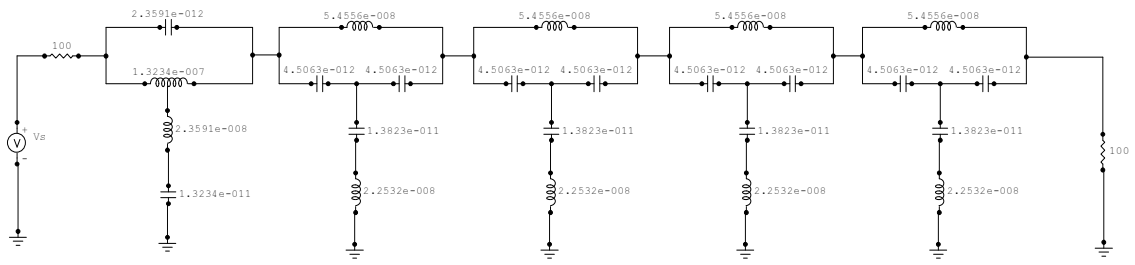

Figure 48 Group delay equalizer circuit for the phase shift network

Similarly, we see that the group delay of the N network shown in the red curve of Figure 49 is not constant over the desired bandwidth. In fact, the group delay of the N network is same as that of the P-network within the desired band since both the networks have a constant phase difference in this band. This can be seen by comparing the curves in Figure 47 and Figure 49 within the desired band 100-900MHz. Hence, we can use the same group delay equalizer circuit given Figure 48. The blue curve in Figure 49 shows the group delay after equalization which has a very small variation of 0.05ns.

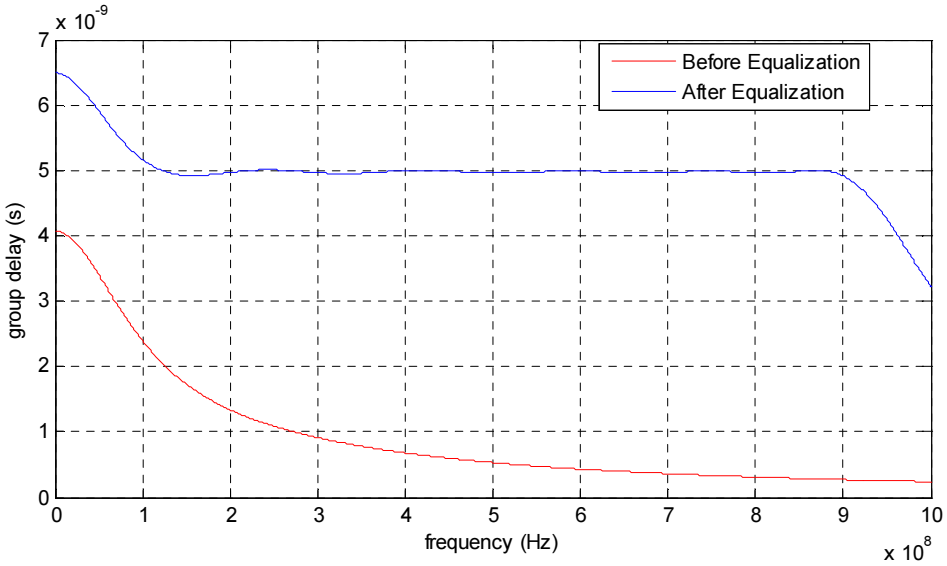

Figure 49 Group delay equalization of the N-network

It would be good future work to actually use this Hilbert transform circuit in the simulation to study the BER performance of the DRB scheme with the delay line and Hilbert transform. According to our simulation with ideal delay and ideal Hilbert transform, BER performance seems to be much better than the case without delay line.

3.6 Decoder (Slicer + Detector)

Ideally, the output digits $\hat{c}_k$ equals –1, 0, or +1 (see the example in Figure 19). We may formulate the following decision rule:

$$\hat{b}_k = \begin{cases} 1 & \text{if } |\hat{c}_k| > 1/2 \\ 0 & \text{if } |\hat{c}_k| < 1/2 \end{cases} \tag{69}$$

When $|\hat{c}_k| = 1$, the receiver makes a random guess in favor of symbol 1 or 0.

CHAPTER 4

CONCLUSION AND POSSIBLE FUTURE RESEARCH WORK

4.1 Conclusion

This thesis gives an overview of phase noise and illustrates its effect on system performance. It discusses the mathematical models of phase noise and a method of phase noise generation using the IEEE recommended model to be used in our simulation. Theoretical phase noise analysis for the BPSK with and without carrier recovery loop was done and simulation results showing the BER performance for various modulation schemes in the presence of the phase noise were also given. These results showed that for a phase noise power of -85dBc/Hz and above at an offset of 1 MHz from the carrier, the BER of the standard schemes like QPSK and QAM-16 increases sharply.

The costas loop which is used for carrier recovery also does not seem to be efficient at GHz range according to our simulation results for phase noise powers higher than -85 dBc/Hz at an offset of 1MHz from the carrier. Hence, we proposed a scheme which employs the pulse-amplitude modulation with the dual-rail bipolar coding. A low power pilot is inserted at the transmitter and recovered at the receiver using a NBPF to be used as a local oscillator to reduce the effect of phase noise.

The NBPF was designed and an analysis of the effect of the bandwidth of the NBPF on the phase noise performance of the DRB system was done to appropriately choose the bandwidth depending on the requirements. The simulation results show that this scheme has a better BER performance than QPSK and QAM-16 schemes for high phase noise powers of -85dBc/Hz and above even without a delay line in the signal path.

Further simulations with an ideal delay line and ideal Hilbert transform showed that the BER performance became even better than the case without delay line. Hence we went on to design a delay line and the Hilbert transform at the receiver end over a bandwidth of 1GHz though these were not actually used in the simulation. The effect of the tolerance values of the passive components was considered and a standard method for electronically tuning the circuits using varactor ICs was suggested to neutralize this effect.

This scheme is novel in the sense of choosing the proper combination of pulse modulation and line coding with a pilot for the sole purpose of mitigating phase noise. We have provided sufficient theoretical explanation and mathematical proof to show that the proposed scheme will effectively improve the phase noise performance of the system and our simulation results also corroborate the conclusions that the BER performance is better than the QPSK and QAM-16 schemes.

Another unique feature of this scheme is that the switching between the different nodes is very fast with a delay only less than 10ns unlike the carrier recovery loops which have a significant locking and tracking time between the nodes whenever they need to switch between different nodes, thus increasing the overall performance of the system.

4.2 Future Research Work

The delay line and Hilbert transform can actually be designed and simulated to see any improvement in the BER performance of the DRB scheme without delay line. It is worthwhile to do this because our simulation with ideal delay and ideal Hilbert transform shows much better BER performance than the case without delay line. Also, the maximum likelihood detection can be implemented for the DRB scheme to get back the inherent 2dB loss of DRB compared to BPSK. This will further improve the BER performance of our scheme. Theoretical phase noise analysis of the DRB scheme can be done to obtain a reasonable BER expression depending on phase noise.

Other than phase noise, another common RF impairment is the non-linearity of the power amplifier. In a typical communication circuit, high power amplifiers are commonly used at the last stage of the transmitter to increase the strength of a transmitted signal. Such amplifiers often operate near saturation and, hence, give rise to nonlinear effects. The nonlinear effects of an amplifier at a specified frequency may be quantified by the amplitude and phase distortions as functions of the amplitude of the input signal. These nonlinear effects can degrade the system performance by increasing the BER across the channel. So, it would be interesting to investigate the BER performance of the dual-rail bipolar system in the presence of the nonlinearity of the power amplifier.

APPENDIX

DUAL-RAIL BIPOLAR VERSUS MODIFIED DUOBINARY

It can be verified that the modulation scheme described in Section 3.2 for each rail is actually equivalent to a PAM transmission system with the *modified duobinary* coding (or the *class IV partial response*) as shown in Figure 50, where a precoding operation is first performed on $\{b_k^{(\mathrm{m})}\}$ to create an intermediate binary sequence $\{d_k^{(\mathrm{m})}\}$ that is defined by

$$d_k^{(\mathrm{m})} = b_k^{(\mathrm{m})} \oplus d_{k-2}^{(\mathrm{m})}, \tag{70}$$

where $\oplus$ denotes the *modulo-two addition* that is equivalent to a two-input *EXCLUSIVE-OR* operation. The precoded binary sequence $\{d_k^{(\mathrm{m})}\}$ ($d_k^{(\mathrm{m})}$ = 0 or 1) is applied to a pulse-amplitude modulator, producing a corresponding two-level sequence of short pulses $\{a_k^{(\mathrm{m})} g(t - kT_\mathrm{b})\}$ whose amplitude $a_k^{(\mathrm{m})}$ is defined by

$$a_k^{(\mathrm{m})} = \begin{cases} +1 & \text{if} \quad d_k^{(\mathrm{m})} = 1 \\ -1 & \text{if} \quad d_k^{(\mathrm{m})} = 0 \end{cases} \tag{71}$$

This sequence of short pulses is next applied to the modified duobinary encoder, thereby producing a three-level sequence $\{c_k^{(\mathrm{m})}\}$ that is related to $\{a_k^{(\mathrm{m})}\}$ as follows:

$$c_k^{(\mathrm{m})} = a_k^{(\mathrm{m})} - a_{k-2}^{(\mathrm{m})} \tag{72}$$

With $a_k^{(\mathrm{m})} = \pm 1$, we find that $c_k^{(\mathrm{m})}$ takes on one of the three values: ±2 and 0. Other than a factor of 2, which results from converting the unipolar sequence $\{d_k^{(\mathrm{m})}\}$ into a polar one, i.e., $\{a_k^{(\mathrm{m})}\}$, the sequence $\{c_k^{(\mathrm{m})}\}$ generated in this manner is exactly same as the one in equation (22).

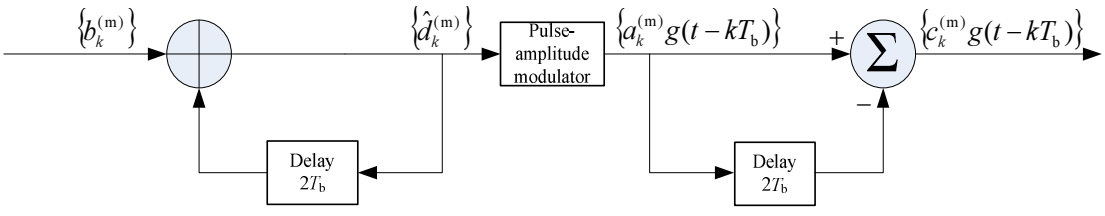

Figure 50 The modified duobinary signaling scheme.

In can be further verified that the combined baseband signal $s(t)$ in equation (23) is equivalent to applying the modified duobinary signaling scheme to the original input binary sequence $\{b_k^{(m)}\}$.

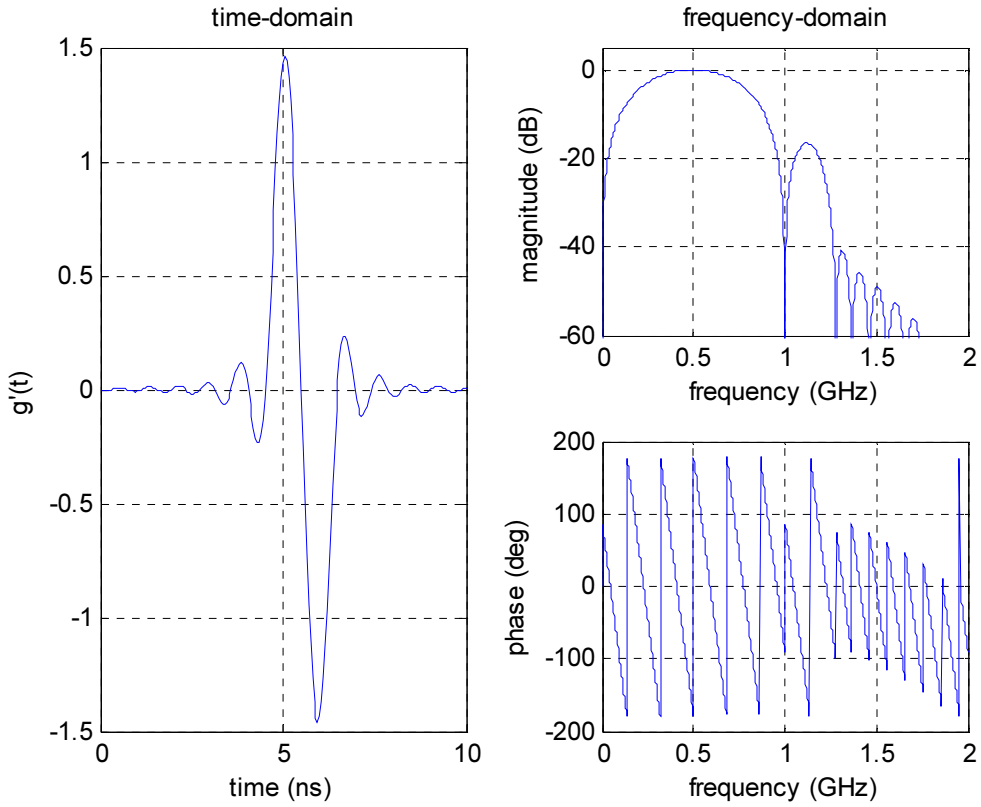

Figure 51 Impulse response of the dual-rail bipolar conversion filter.

Therefore $s(t)$ can also be expressed as

$$s(t) = \sum_k c_k g(t - kT_b), \tag{73}$$

where c_k is defined through equations (70) to (72) without superscripts. Making use of equation (72), equation (73) can be further written as

$$s(t) = \sum_k a_k g'(t - kT_b), \tag{74}$$

where $g'(t) = g(t) - g(t - 2T_b)$ can be treated as the impulse response of the modified duobinary conversion filter, or equivalently the dual-rail bipolar conversion filter, and its Fourier transform is given by:

$$G'(f) = 2j \sin(2\pi f T_b) \exp(-j2\pi f T_b) G(f) \tag{75}$$

Figure 51 shows a plot of $g'(t)$ in both time- and frequency-domains with $g(t)$ being the square-root raised-cosine pulse shown in Figure 9. Notice that $\left|G'(f)\right|^2$ is exactly same as $S(f)$ with $p = 0.5$ in equation (25) except for a constant factor.

BIBLIOGRAPHY

[1] Best, R. E., Phase-Locked Loops: Design, Simulation, and Applications (5th Edition), McGraw-Hill, Inc., New York, June 2003.

[2] Choi, C. S., et. al., RF Impairment Models for 60GHz-Band SYS/PHY Simulation, IEEE Document 802.15-06-0477-01-003c, November 2006.

[3] Dowla, F., Handbook of RF & Wireless Technologies, Elsevier, Inc., New York, October 2003.

[4] Franks, L. E., Signal Theory, Prentice-Hall, Inc., New Jersey, 1969.

[5] Gardner, F. M., Phaselock Techniques (2nd Edition), John Wiley & Sons, Inc., New York, April 1979.

[6] Hajimiri, A. and T. H. Lee, A General Theory of Phase Noise in Electrical Oscillators, IEEE J. of Solid-State Circuits, Vol. 33, No. 2, February 2000.

[7] Haykin, S., Communication Systems (4th Edition), John Wiley & Sons, Inc., New York, May 2000.

[8] Jeruchim, M. C., Philip, B. and Sam, K. S. Simulation of Communication Systems (2nd Edition), Kluwer Academc/Plenum Publishers, New York, 2000.

[9] Lee, T. H. and A. Hajimiri, Oscillator Phase Noise: A Tutorial, IEEE J. of Solid-State Circuits, Vol. 35, No. 3, March 2000.

[10] Lee, T. H., Planar Microwave Engineering: A Practical Guide to Theory, Measurements and Circuits, Cambridge University Press, August 2004.

[11] Leeson, D. B., A Simple Model of Feedback Oscillator Noise Spectrum, Proc. IEEE, Vol. 54, February 1966.

[12] Oppenheim, A. V., R. W. Schafer, and J. R. Buck, Discrete-Time Signal Processing (2nd Edition), Prentice Hall, Inc., New Jersey, February 1999.

[13] Papoulis, A. and S. U. Pallai, Probability, Random Variables and Stochastic Processes (4th Edition), McGraw-Hill, Inc., New York, January 2002.

[14] Proakis, J. G., Digital Communications (4th Edition), McGraw-Hill, Inc., New York, August 2000.

[15] Rael, J. J. and A. A. Abidi, Physical Processes of Phase Noise in Differential LC Oscillators, Proceedings of IEEE Custom Integrated Circuits Conference, May 2000.

[16] Razavi, B., A Study of Phase Noise in CMOS Oscillators, IEEE J. of Solid-State Circuits, Vol. 31, No. 3, March 1996.

[17] Trees, H. L. V., Detection, Estimation, and Modulation Theory Part II: Nonlinear Modulation Theory, John Wiley & Sons, Inc., New York, June 1971.

[18] Ziemer, R. E. and R. L. Peterson, Introduction to Digital Communication (2^{nd} Edition), Prentice Hall, Inc., New Jersey, August 2000.

[19] Williams, A. B. and Taylor, F. J., Electronic Filter Design Handbook (4^{th} Edition), McGraw Hill, New York, 2006.

[20] Stephens, D. R., Phase-locked loops for wireless communications (2^{nd} Edition), Kluwer Academic Publishers, New York, 2002.

[21] Choi, T.,Lee, H., Katehi, L. P. B., and Mohammadi, S., A Low Phase Noise 10 GHz VCO in 0.18 μm CMOS Process

[22] Eo Y., K. Kim, and B. Oh, “Low noise 5 GHz differential VCO using InGaP/GaAs HBT technology,” IEEE Microw.Wireless Compon. Lett., vol. 13, no. 7, pp. 259–261, Jul. 2003.
[23] Baek D. H., S. Ko, J. G. Kim, D. W. Kim, and S. Hong, “Ku-Band InGaP-GaAs HBT MMIC VCOs with balanced and differential topologies,” IEEE Trans. Microw. Theory Tech., vol. 52, no. 4, pp. 1353–1359, Apr. 2004.
[24] Zirath H., R. Kozhuharov, and M. Ferndahl, “Balanced Colpitt oscillator MMICs designed for ultra-low phase noise,” IEEE J. Solid-State Circuits, vol. 40, no. 10, pp. 2077–2086, Oct. 2005.
[25] Meng C. C., C. H. Chen, Y. W. Chang, and G. W. Huang, “5.4 GHz–127 dBc/Hz at 1 MHz GaInP/GaAs HBT quadrature VCO using stacked transformer,” Electron. Lett., vol. 41, no. 16, pp. 906–908, Aug. 2005.
[26] Lenk F., M. Schott, J. Hilsenbeck, and W. Heinrich, “A new design approach for l ow phase-noise reflection-type MMIC oscillator,” IEEE Trans. Microw. Theory Tech., vol. 52, no. 12, pp. 2725–2731, Dec.2004.
[27] Baek D., T. Song, E. Yoon, and S. Hong, “8-GHz CMOS quadrature VCO using transformer-based LC-based LC tank,” IEEE Microw. Wireless Compon. Lett., vol. 13, no. 10, pp. 446–448, Oct. 2003.
[28] Kwok K. and H. C. Luong, “Ultra-low-voltage high-performance CMOS VCOs using transformer feedback,” IEEE J. Solid-State Circuits, vol. 40, no. 3, pp. 652–660, Mar. 2005.
[29] Lindsey W. C. and M. K. Simon, Telecommunication Systems Engineering. Englewood Cliffs, NJ: Prentice-Hall, 1973.
[30] Lindsey W. C., "Phase-shift-keyed signal detection with noisy reference signals," IEEE Trans. Aerosp. Electron. Syst., vol. 2, no. 4, pp. 393-401, July 1966.
[31] Jain P. C. and Blachman N. M., "Detection of a PSK signal transmitted through a hard-limited channel," IEEE Trans. Inform. Theory, vol. 19, no.5, pp. 623-630, Sept. 1973.
[32] Prabhu V. K., "PSK performance with imperfect carrier phase recovery," IEEE Trans. Aerosp. Electron. Syst., vol. 12, no. 2, pp. 275-285, Mar. 1976.
[33] Kam P. Y., S. K. Teo, Y. K. Some and T. T. Tjhung, "Approximate results for the bit error probability of binary phase shift keying with noisy phase reference," IEEE Trans. Comm., vol. 41, no. 7, pp. 1020-1022, July 1993.
[34] Blachman N. M., "The effect of phase error on DPSK error probability," IEEE Trans. Comm., vol. 29, no. 3, pp. 364-365, Mar. 1981.
[35] Kam P. Y., K. Y. Seek, T. T. Tjhung and P. Sinha, "Error probability of 2DPSK with phase noise," IEEE Trans. Comm., vol. 42, no. 7, pp. 2366-2369, July 1994.
[36] Hamaguchi, K.; Shoji, Y.; Ogawa, H., “BER performance of coherent-QPSK transmissions affected by phasenoise from frequency converters” IEEE Vehicular Technology Conference, vol. 4, pp. 2281 – 2284, 2001
[37] Weber W. J., III, "Performance of phase-locked loops in the presence of fading communication channels," IEEE Trans. Comm., vol. 24, no. 5, pp. 487-499, May 1976.
[38] Bateman A. J. and J. P. McGeehan, "Data transmission over UHF fading mobile radio channels," IEE Proc. F, vol. 131, no. 4, pp. 364-374, July 1984.

[39] Yokoyama M., "BPSK system with sounder to combat Rayleigh fading in mobile radio communication," IEEE Trans. Veh. Technol., vol. 34, no. 1, pp. 35-40, Feb. 1985.
[40] Bateman A., "A general analysis of bit error probability for reference-based BPSK mobile data transmission," IEEE Trans. Comm., vol. 37, no. 4, pp. 398-402, Apr. 1989.
[41] Zhang Y., V. K. Dubey and J. S. Fu, "Error probabilities for coherent BPSK and QPSK in a slowly flat fading Rayleigh channel with random phase noise," Journal of Electrical and Electronics Engineering, Australia, vol. 19, no. 3, pp. 123-128, Sept. 1999.
[42] Lindsey W. C., "Phase-Shift-Keyed Signal Detection with Noisy Reference Signals," IEEE Transactions on Aerospace and Electronic Systems, July 1966, pp 393-401
[43] Lindsey W. C., M. K. Simon, Telecommunication Systems Engineering, Prentice-Hall, 1972
[44] Lindsey W. C., K. Tu, "Phase Noise Effects on Space Shuttle Communications Link Performance," IEEE Transactions on Communications, Vol COM-26, No 11, November 1978, pp 1532-1541
[45] Stiffler J. J., Theory of Synchronous Communications, Prentice-Hall, 1971, pp 268-272.
[46] Prabhu V.K., "PSK Performance with Imperfect Carrier Recovery Phase," IEEE Transactions on Aerospace and Electmnic Systems, March 1976, pp 275-286
[47] Holmes J.K., Coherent Spread Spectrum Svstems, New York, Wiley, 1982
[48] Daryanani G., Principles of Active Network Synthesis and Design, John Wiley and sons, New York, 1976.
[49] http://www.ieee802.org/15
[50] Fisher R., "60 GHz WPAN Standardization within IEEE 802.15.3c", International Symposium on Signals, Systems and Electronics, 2007. ISSSE '07.
[51] Guo N., Qiu R. C., Mo S. S., Takahashi K., "60-GHz Millimeter-Wave Radio: Principle, Technology, and New Results", EURASIP Journal on Wireless Communication and Networking", 2007.
[52] Olbrich M. O., L. Huang, E. M. Biebl, " A varactor tuned low-cost 24GHz harmonic VCO", Advances in Radio Science, Germany 2006.
[53] Hilliker S., J. Alberkrack, "A medium-cost PLL varactor tuning system utilizing off-the-shelf logic", IEEE transactions on Broadcast and Television Receivers, 1974.
[54] Razavi B., RF Microelectronics, Prentice Hall, New Jersey, 1998.
[55] Lee T. H., The Design of CMOS Radio-requency Integrated Circuits (2nd Edition), Cambridge University Press, 2004.
[56] http://www.americanmicrosemi.com